

# Experimental study of three-dimensional turbulence under a free surface

Timothée Jamin,\* Michael Berhanu, and Eric Falcon  
*Université Paris Cité, MSC, UMR 7057 CNRS, F-75013 Paris, France*  
(Dated: February 1, 2024)

In many environmental flows, an air-water free surface interacts with a turbulent flow in the water phase. To reproduce this situation, we propose an original experimental setup, which is an evolution of the Randomly Actuated Synthetic Jet Array (RASJA) device used to study turbulence with a low mean flow. By using a central pump connected to jets, we generate a turbulent flow of tunable intensity with good isotropy and horizontal homogeneity. The maximal turbulent Reynolds number of 8800 is significantly larger than in other systems generating turbulence with low mean flow, including RASJA experiments, for which the flow rate per jet cannot be changed. Using our setup, we characterize the modification of the turbulence under the influence of the free surface, which acts typically for depths smaller than the integral length measured in the bulk. We report that the turbulent fluctuations become strongly anisotropic when approaching the free surface. The vertical velocity fluctuations decrease close to the surface whereas the horizontal ones increase as reported in previous theoretical predictions and numerical observations. We also observe a strong enhancement of the amplitude of the temporal and spatial power spectra of the horizontal velocity at large scales, showing the strengthening of these velocity fluctuations near the free surface.

## I. INTRODUCTION

Turbulence is ubiquitous in most environmental flows of water like the sea currents, the rivers, or the streams. The specificity of all these examples, compared to the classic three-dimensional turbulence [1–4], consists in the presence of a top-free surface at the interface between the liquid and the atmosphere. The behavior of this deformable and renewable interface constitutes a very complex problem, especially in the presence of turbulence in the liquid phase. Brocchini and Peregrine proposed a qualitative description of the turbulent dynamics of a free surface [5]. The deformation of the free surface results from the respective contributions of the pressure field, viscous stresses associated with the vorticity, and propagation of surface waves, which correspond to the natural response of the interface to perturbations. The free surface acquires roughness, can break up, and can disintegrate forming droplets. This last case considerably increases gas, heat, and mass exchanges between the atmosphere and the water body. This problem of considerable environmental importance [6] has thus deserved several studies in the field [7], with controlled experiments [8, 9] or using numerical simulations [10].

Facing the complexity of the dynamics of a turbulent free surface, the first step consists in fundamentally understanding the behavior of hydrodynamic turbulence in the vicinity of a free surface. We can distinguish two standard cases depending on whether turbulence is accompanied by a mean flow. In the first case, several studies have investigated open channel flows numerically [11–13] and experimentally [14]. The degree of turbulence can also be enhanced using an active grid [15, 16] or a rough bed in shallow water [17]. For large fluid depth, the ratio of velocity fluctuations to the mean flow remains below 10%, even using an active grid.

In this study, we focus on the second case, i.e., the absence of a mean flow. In this situation, several numerical simulations have investigated homogeneous and isotropic turbulence in the vicinity of a free-slip top interface in a decaying regime or with sustained forcing [10, 18–22]. To approach natural and experimental configurations, few studies have also investigated the case of a free surface contaminated by surfactants [23–25]. Finally, to our knowledge, turbulent flows deforming a top free surface have been little addressed and only numerically [26, 27]. Two main results can be summarized from the previous studies. First, near the free surface, the vertical velocity fluctuations are significantly reduced whereas the horizontal ones are enhanced. The rapid distortion theory (RDT) can explain this effect [28–30]. Secondly, for a high enough Reynolds number, the power spectrum of the horizontal velocities follows the power law in  $k^{-5/3}$  predicted by Kolmogorov for isotropic homogeneous turbulence [1, 3] even close to the free surface despite the flow anisotropy. Some experimental studies report this power law close to the free surface from field observations on the surface of a river [31, 32] and in laboratory experiments with a grid-stirred tank [8, 33]. This observation may be explained by an analogy with stratified turbulence [22].

Most of the experiments investigating the interaction between the turbulence with low mean flow and a free surface use an oscillating grid to generate turbulence [33–37], where a horizontal grid plunged in the tank below the free

---

\* E-mail: [research@timotheejamin.com](mailto:research@timotheejamin.com)

surface is vertically oscillated. Unfortunately, these devices have experimental repeatability issues [38] and the level of turbulence remains moderate: typically the root mean square (rms) velocity is below or equal to  $5 \text{ cm s}^{-1}$  for a meter scale experiment. The such-generated flows display also large-scale correlations due to the grid oscillation. Large-scale perturbations of the free surface would be also expected by a turbulent flow produced by the motion of impellers like for the von Kármán closed flows [39–41] or by the erratic motion of small magnetically-driven particles [42]. However, these methods with inertial forcing have not been used for now to study turbulence in the vicinity of a free surface. Recently, a turbulent free-surface flow has been obtained using a magnetohydrodynamic forcing at small scale [43]. Nevertheless, to ensure a sufficient level of turbulence, magnetohydrodynamically driven flows require the use of liquid metals, for which hydrodynamics measurements are difficult due to the opacity of the liquid. Moreover, flows generated by this method are intrinsically anisotropic.

Finally, to our knowledge, the best method to investigate turbulence near a free surface in the laboratory consists in using a water tank randomly stirred by synthetic jets placed at the bottom of the tank. This configuration introduced and characterized by E. Variano, E. Bodenschatz, and E. Cowen [44, 45] displays a turbulent flow featuring high-Reynolds-number, large-scale isotropy, homogeneity and a ratio between mean and fluctuating flow less than 10%. Like in the previous studies using an oscillating grid [33, 37], the decay of vertical fluctuations when approaching the free surface is in qualitative agreement with the predictions of the RDT [19, 28, 30]. In recent years, random jet arrays have become a popular method to generate homogeneous isotropic turbulence with low mean flow in air and water using various configurations of the array [46–50] and different driving algorithms firing the jets [51]. However, for experiments in water, jets are produced by numerous (from 60 to 128) inexpensive immersed small pumps, which are set on or off according to a firing pattern. Consequently, as the flow rate of each pump depends on its working point, the global intensity of the turbulence cannot be varied. We note also that turbulence in the presence of a free surface has been investigated in a jet-agitated vessel [52, 53] to measure gas-liquid transfers. One hundred vertical nozzles at the bottom are connected to a large pump. However, with jets running continuously, secondary motions very sensitive to initial conditions induce the presence of a non-negligible mean flow [53].

Here, we introduce a new method to generate homogeneous isotropic turbulence in a water tank, in order to experimentally study the interaction between hydrodynamic turbulence and a deformable free surface. The experimental device is an evolution of the Randomly Actuated Synthetic Jet Array (RASJA) device [44, 45]. A large pump with an adjustable and regulated flow rate is connected with an array of 64 solenoid valves controlled independently. By varying the global flow rate, a large range of levels of turbulence can be obtained in a water tank of  $40 \times 40 \times 75 \text{ cm}$  while keeping a good level of homogeneity and isotropy for an appropriate choice of open jet duration and firing pattern. Using this device, we characterize the near-surface turbulence and fruitfully complete existing works. The study of free-surface deformation induced by turbulence [26] will be the object of subsequent work. The paper is organized as follows. Section II describes the experimental setup and the methods to generate nearly homogeneous and isotropic turbulence with a small mean flow in a water tank. In Sec. III, we characterize the turbulence far from the free surface for the best choice of the jet pattern. Then, Sect. IV investigates the modification of the turbulence when the free surface is approached. We give our conclusions and perspectives in Sec. V.

## II. EXPERIMENTAL SETUP

### A. A randomly actuated synthetic jet array with a tunable flow-rate

The RASJA device proposed by Variano and Cowen [45] generates a turbulent flow with small mean flow. It consists of a  $8 \times 8$  array of jets firing upwards at the bottom of a tank in the presence of a free surface. Each of the 64 jets is driven by a submerged centrifugal pump which is alternatively turned on and off in a spatio-temporal random pattern in such a way that only a fraction of the jets are firing simultaneously. The produced turbulent flow has a low mean flow and displays excellent results in terms of horizontal homogeneity, isotropy, and reproducibility. It also reaches a turbulent Reynolds number 7 times higher than those reached with oscillating grids. However, the pumps have a fixed flow rate, and thus varying the intensity of turbulence is difficult. The intensity of turbulence may only be tuned by changing the water depth, the average number of simultaneous jets, or the average time for which a jet remains on. But this would also affect the flow characteristics such as the typical size of eddies [54].

In order to reach various levels of turbulence in an independent way, we propose in this paper a variation of the RASJA device. The jets are supplied by only one central centrifugal pump with a high flow rate and each jet is individually driven by a solenoid valve which turns the jet on or off by being respectively open or closed. Due to the central high flow rate of the pump, the turbulence intensity can be varied over a large range of Reynolds numbers. Consequently, higher levels of turbulence are reached than with the original RASJA device (see Sect. III D). This feature is of primary importance for our setup as the final objective consists in characterizing different regimes of surface deformation as a function of the subsurface Reynolds number. A similar configuration had been used by

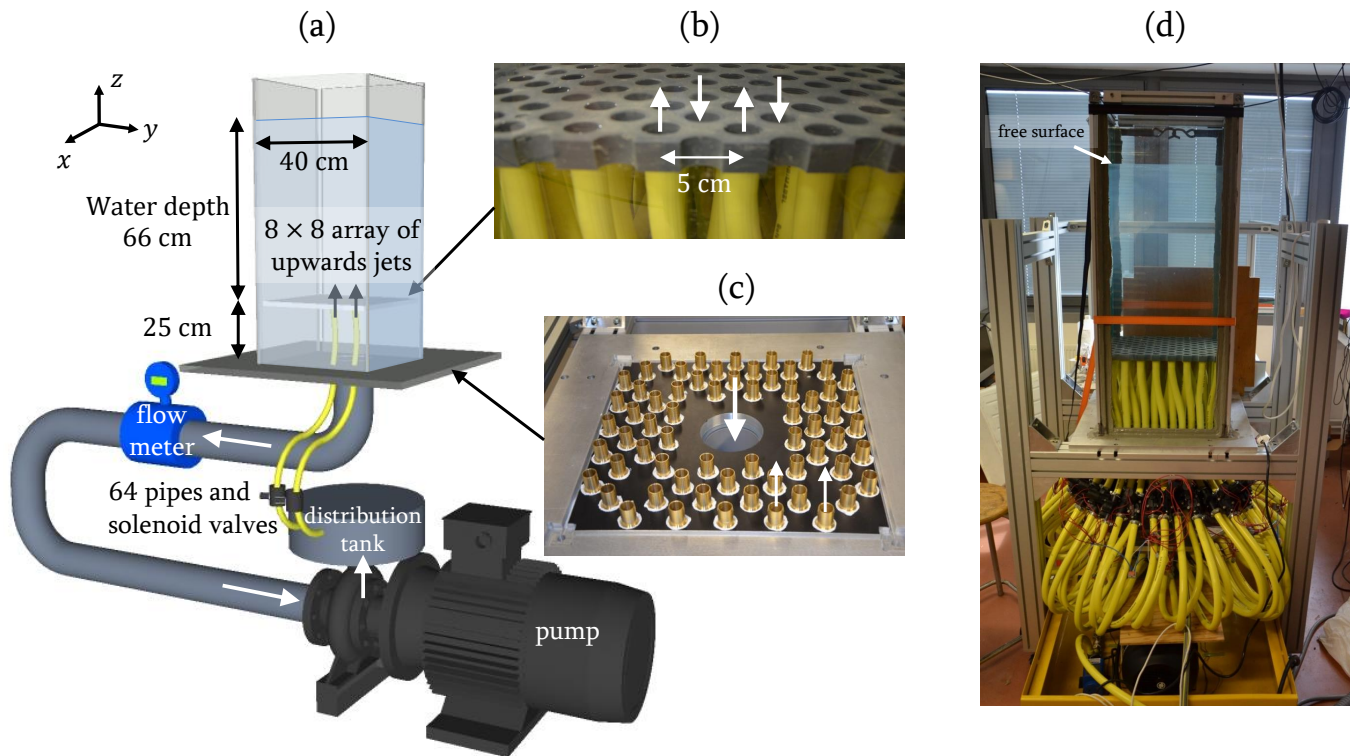


FIG. 1. (a) General schematic diagram of the experimental setup used to produce turbulence. The turbulent flow is generated in a square glass tank of side 40 cm filled with water to a depth of 66 cm. (b) Close-up view of the 64-jet grid (up arrows) with a 5-cm spacing placed 25 cm above the tank bottom. Down arrows correspond to suction holes. (c) View of the tank bottom before connecting the pipes. Jets are arranged around a central suction hole. (d) Global view of the experimental setup.

Variano *et al.* as a prototype with 9 jets [44] and by Delbos *et al.* [55], but using 4 solenoid valves only to control 64 jets. None of these two studies fully characterized the obtained turbulence.

In our setup, the turbulence is produced with 64 jets in a glass tank, which is  $40 \times 40 \text{ cm}^2$  wide and 100 cm high [see Fig. 1 (a)]. The jets are placed 25 cm above the tank bottom and are firing upwards. They are arranged in a  $8 \times 8$  array with a spacing of 5 cm. The flow is produced by a unique centrifugal pump. The outlet port of the pump is facing up and is connected to a cylindrical redistribution chamber which is 12 cm high and has a diameter of 40 cm. Pipes are connected to 64 hose connections arranged on two rows at the periphery of the chamber. A solenoid valve is mounted on each pipe to individually turn on or off each jet according to a random spatio-temporal pattern (see Sect. II B below). The other pipe ends are connected to the glass tank from below and are arranged around a 80 mm-diameter hole [see Fig. 1 (c)]. This central hole is connected to the inlet port of the pump through a PVC (PolyVinyl Chloride) pipe equipped with a flow meter so that the water is in a closed system. A PVC slab is placed 25 cm above the bottom of the tank and is connected to it with pipes to redistribute the jets. This way, they are in a  $8 \times 8$  array, with a 5 cm square mesh size and a 16.5 mm inside diameter [see Fig. 1 (b)]. Suction holes of 25 mm in diameter are carved in the PVC slab at the center of each square formed by inlet jets.

By initially filling the tank, the water depth can be adjusted until 75 cm, which is the distance from the plate with the jets to the top of the tank. In the experiments described in this article, the water depth is set to 66 cm. Like other RASJA experiments, this device is a closed hydraulic circuit and the amount of water in the tank is constant. With this experimental setup, we are able to tune the level of turbulence by changing the flow rate of the centrifugal pump. This was not the case with the RASJA setup of Variano and Cowen [45] as the bilge pumps have no variable flow rate. Our powerful pump is a 7.5 kW Grundfos NB 65-125/137 (AFA BAQE). It can reach a pressure of 2.4 bars or a flow rate of  $38 \text{ L s}^{-1}$  at a pressure of 1.6 bars. The flow rate is controlled using a feedback loop with a flow meter (Mecon mag-flux A) and a frequency driver (Inorea Powtran PI8100 11 kW). The frequency driver sets the power of the pump by varying input voltage and frequency.

## B. Algorithm to produce random spatiotemporal jet opening

Solenoid valves make each jet independent so that they can be turned on or off according to a random spatiotemporal pattern to produce hydrodynamic turbulence. We chose internally piloted solenoid valves Irritrol 700B-.75 Ultra Flow, which display large orifices and thus low-pressure drops (e.g., 0.15 bar for a 1-L s<sup>-1</sup> flow rate). A small plastic piece inside the solenoid valve, initially aiming at avoiding a water hammer effect, was removed to decrease the opening and closing times of the valves to about 1 s. While we use 64 identical solenoid valves, we observe variability in the individual flow rates probably due to serial effects. For example, a standard deviation of 0.042 L s<sup>-1</sup> was measured for a jet mean flow  $Q_j = 0.13 \text{ L s}^{-1}$  [56]. The jets were arranged in a configuration for which the distribution of flow rates is symmetrical and as homogeneous as possible so that we avoid local mean flows. Solenoid valves are powered with two 400-W power transformers with a 24-VAC and 50-Hz voltage. They are triggered with two Arduino Mega 2560 microcontrollers and solid-state relays (Measurement Computing SSR-4-OAC-05).

We use an algorithm to optimize turbulence intensity and minimize local mean flows. Opening and closing times of each solenoid valve are set by the algorithm, for which only a fraction of the 64 jets is simultaneously open. With the “sunbathing algorithm” developed and used by Variano and Cowen [45], each jet is independently governed by randomly picking up successive opening and closing durations. This way, while the average number of jets firing at the same time is chosen, the number of jets firing at any instant is not constant. This algorithm displays low mean flow, high Reynolds number and good spatial homogeneity and has been used in most of subsequent RASJA experiments [47–50]. However, as our experimental setup involves a unique centrifugal pump, the flow rate should be kept constant. Thus, in this paper, we use a pattern very close to the constant-momentum input algorithm mentioned by Variano and Cowen [45] who report performance similar to the “sunbathing algorithm”. In our algorithm, the number of jets  $N_{on}$  firing at the same time remains constant and the opening time is chosen at each time within a uniform distribution  $f_{on}$  of mean value  $\mu_{on}$  and half-width  $\sigma_{on}$ . Initially,  $N_{on}$  jets are randomly chosen. Each one is open during a time  $d_{on}$  randomly chosen between 0 and  $\mu_{on} \pm \sigma_{on}$ . Each time a jet reaches the end of its opening duration, it is replaced by a jet randomly picked up from closed ones for which a new opening time  $d_{on}$  is randomly chosen from the uniform distribution  $f_{on}$ .

As a solenoid valve needs around 1 s to reach a satisfying flow rate, we choose  $\mu_{on} = 3 \text{ s}$  and  $\sigma_{on} = 1 \text{ s}$  like Variano and Cowen [45]. These authors also found that the highest level of turbulence is reached for  $N_{on} = 8$  jets open at the same time. Due to the variability in the individual flow rates of the solenoid valves mentioned above, we choose  $N_{on} = 16$  to keep the global flow rate more constant in time and homogeneous in space.

## C. Measurement techniques

The velocity field under the free surface is measured using Particle Image Velocimetry (PIV). A continuous laser sheet passing through the basin center illuminates a vertical slice of water seeded with 20- $\mu\text{m}$  Polyamid Seeding Particles (PSP). A high-speed camera (Phantom V10) images a two-dimensional domain in the illuminated region with a resolution of  $2400 \times 720$  pixels. In the following, the measurement domain located in the vertical plane at  $y = 0$  corresponds to  $x \in [-15, 15] \text{ cm}$  for the horizontal coordinate and to  $z \in [-9, 0] \text{ cm}$  for the vertical coordinate.  $z = 0$  is the position of the top free surface and the point  $(x = 0, y = 0)$  is the horizontal center of the square tank. Spatial measurements needing a statistical convergence are obtained by computing one velocity field per second for 1800 s, with a 2-ms time interval between images of a pair. Velocity vectors are computed using the PIVLab plugin for Matlab [57] in a grid of  $4 \times 4\text{-mm}^2$  windows with a 2 mm mesh size. We denote  $u$  and  $w$  the instantaneous local velocities in the horizontal (along  $x$  coordinate) and vertical (along  $z$  coordinate) directions of the measurement plane, respectively. Their local time-averaged values are  $U(x, y, z) = \overline{u(x, y, z, t)}$  and  $W(x, y, z) = \overline{w(x, y, z, t)}$ , respectively. The velocity component  $v$  (along  $y$  coordinate) is perpendicular to the measurement plane and it is thus not measured. Velocity fluctuations are characterized by their standard deviations  $\sigma_u$  and  $\sigma_w$ , with  $\sigma_u = \sqrt{u^2 - U^2}$ .

The characterization of the velocity field is completed with Laser Doppler Velocimetry (LDV) measurements performed with a Dantec Dynamics FlowExporer 1D apparatus. This local measurement is also performed by seeding water with 20- $\mu\text{m}$  PSP. The velocity temporal signal is interpolated to obtain a constant sampling frequency of 1000 Hz. All LDV measurements are performed in  $x = 0$  and for various  $z$ , while two positions are used for  $y$  (0 and  $-7 \text{ cm}$ ), the uncentered one being able to reach smaller depths for vertical measurements as it is less restricted by the constraint of non-intersection between the laser beams and the free surface.

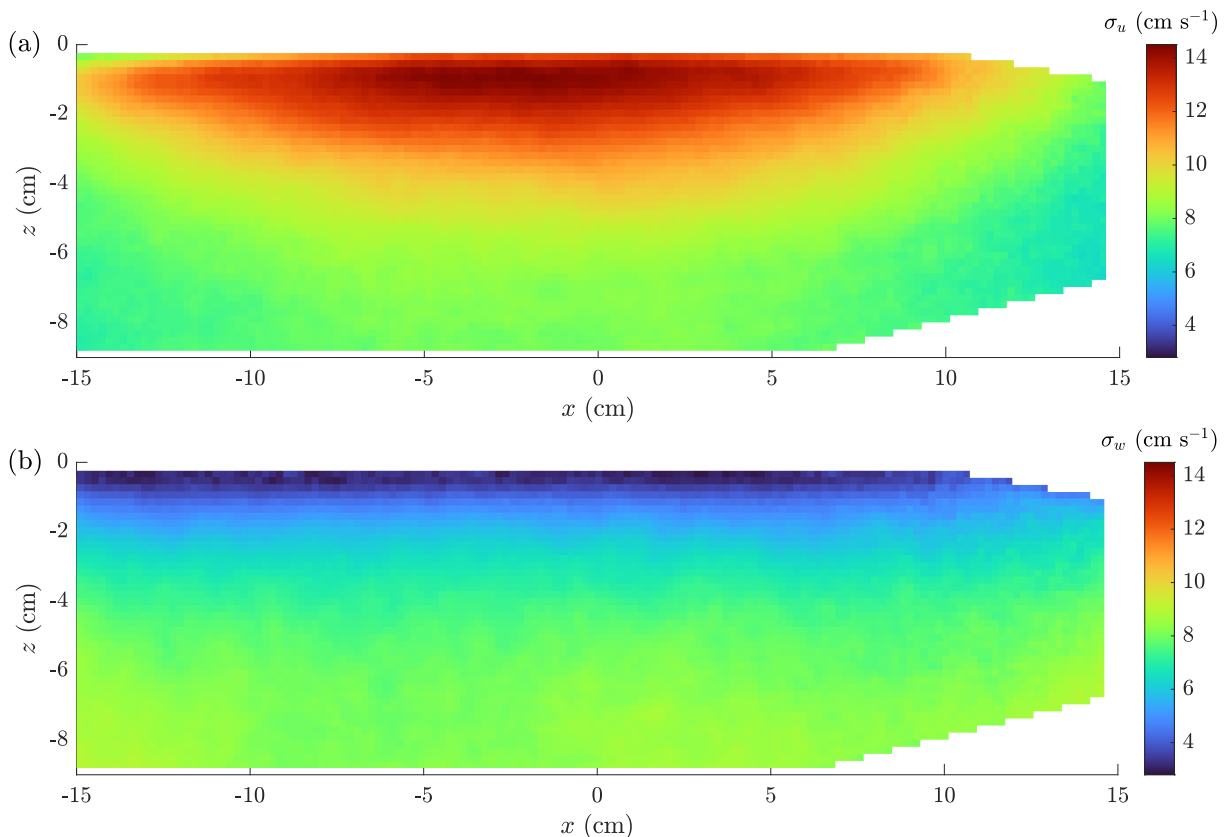


FIG. 2. Standard deviations of (a) horizontal and (b) vertical velocity fluctuations,  $\sigma_u$  and  $\sigma_w$  respectively, in the vertical plane at  $y = 0$  cm using Particle Image Velocimetry (PIV). White regions are regions not lighted by the laser sheet. Parameters of Experiment A. The free surface is located at  $z = 0$ .

#### D. General features of generated turbulent flows

The turbulent flows generated with our device correspond to 16 jets (over 64) open at the same time, each remaining open for an average time of 3 s, with a mean flow rate per jet  $Q_j$  varying between  $0.06$  and  $0.56$  L  $s^{-1}$  and a water depth of 66 cm. In these conditions, we obtain turbulent flows with a low mean flow, a satisfying homogeneity, and a good isotropy except in the vicinity of the jets and of the free surface, similar to the previous RASJA experiments. Colormaps of velocity fluctuations  $\sigma_u$  and  $\sigma_w$  are displayed in Fig. 2 for the Experiment A, a typical case corresponding to a flow rate per jet  $Q_j = 0.375$  L  $s^{-1}$  (characteristics are available in Table II). Notice that the top and bottom-right corners are not illuminated so full-width measurements are available for  $z \in [-7; -1.2]$  cm only.

The region of interest is sufficiently far from the bottom plate, to not observe the signature of individual jets in the velocity field. We observe that horizontal velocity fluctuations are maximal near the free surface and the horizontal center of the tank while vertical velocity fluctuations decrease when approaching the free surface. Figure 3 (a) shows the horizontal velocity profile, computed from Fig. 2 averaged over  $z \in [-7.4; -6]$  cm.  $\sigma_u$  and  $\sigma_w$  display good isotropy and homogeneity, in particular for  $-5 < x < 5$  cm. When coming closer to the free surface (see Fig. 3 (b), same as (a) but averaged over  $z \in [-1.7; -0.2]$  cm), the homogeneity stands for  $\sigma_w$  while lateral boundaries affect  $\sigma_u$ . This latter phenomenon is because eddies are horizontally elongated, as will be studied and detailed in Sect. IV.

Besides, Fig. 4 displays the vertical profile of velocity fluctuations using LDV individual measurements, including measurements below the PIV domain (vertical PIV profile will be studied in Sect. IV). While turbulent intensity decays when moving away from the forcing region, a plateau is formed for depth between  $-10$  and  $-6$  cm, similar to Variano and Cowen [45] observations. The plateau is also consistent with the homogeneous regions visible on the lower parts of Figs. 2 (a) and (b).

The region defined by  $-5 < x < +5$  cm and  $-9 < z < -6$  cm displays a very good homogeneity on these figures. Indeed, the standard deviation of  $\sigma_u$  and  $\sigma_w$  over this region is equal to 2.4% and 2.3% of  $\sigma_u$  and  $\sigma_w$  respectively when averaging over all measurements (and below 3.6% for each measurement). So the turbulence intensity will now be quantified by averaging  $\sigma_u$  and  $\sigma_w$  over this region. These averaged values  $\tilde{\sigma}_u$  and  $\tilde{\sigma}_w$  are plotted as functions of

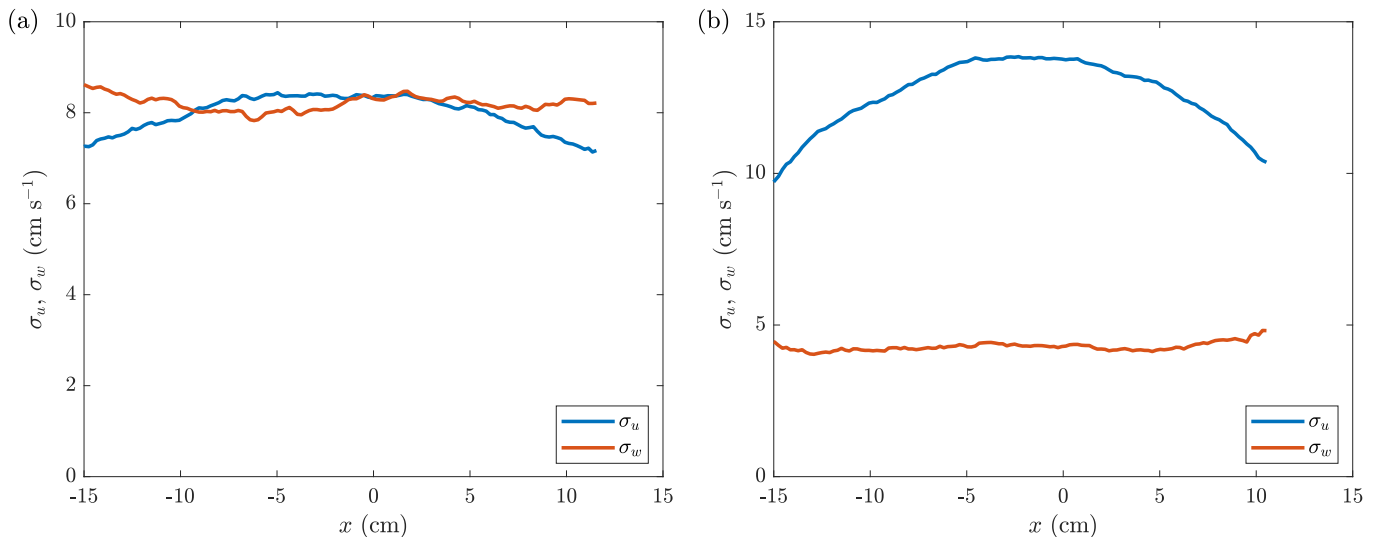


FIG. 3. Horizontal profiles of standard deviations for horizontal and vertical velocity fluctuations  $\sigma_u$  and  $\sigma_w$ , averaged vertically (a) in the nearly-homogeneous region ( $-7.4 \leq z \leq -6$  cm) and (b) close to the free surface ( $-1.7 \leq z \leq -0.2$  cm). Parameters of Experiment A.

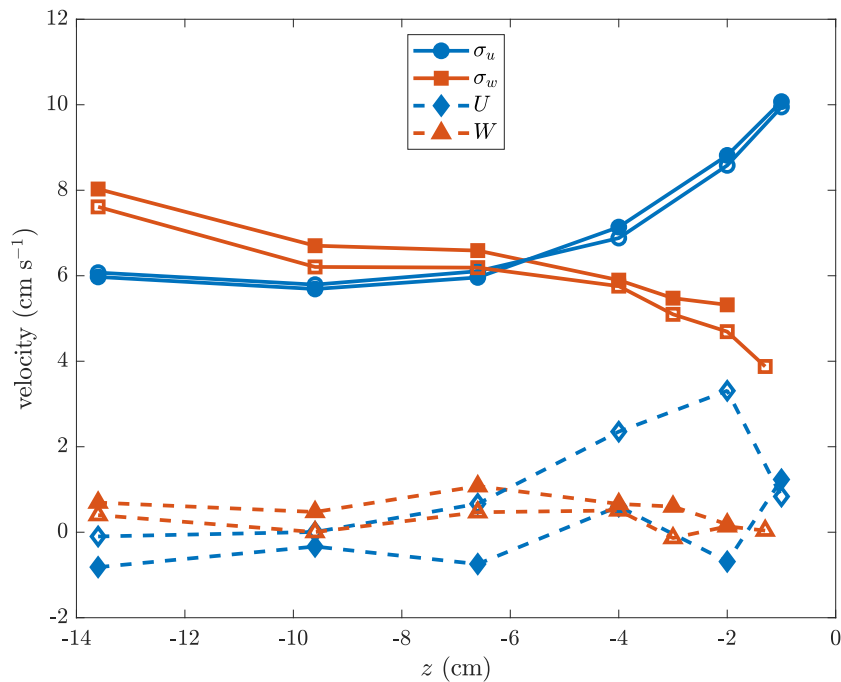


FIG. 4. LDV measurements of standard deviations  $\sigma_u$  and  $\sigma_w$  and mean flows  $U$  and  $W$  for horizontal and vertical velocities as functions of  $z$ . Each point is an independent measurement of 1200-s duration.  $Q_j = 0.25 \text{ L s}^{-1}$ ,  $x = 0$  and  $y = 0$  (filled symbols) or  $y = -7$  cm (empty symbols).

the flow rate per jet  $Q_j$  in Fig. 5 and reported in Table I.

We observe that, beyond homogeneity, this region displays a good isotropy, i.e.,  $\tilde{\sigma}_u \approx \tilde{\sigma}_w$ , for all the flow rates. The local anisotropy ( $\tilde{\sigma}_w/\tilde{\sigma}_u \in [0.90; 1.01]$  over all the experiments) is lower than the value measured by Variano and Cowen [45] (value of 1.27) or reported by the same authors from others studies (values between 1.1 and 1.4 for grid-stirred tanks). We can see in Fig. 4 that the anisotropy out of the region defined by  $-9 < z < -6$  cm is larger. This good local isotropy is thus obtained thanks to the presence of the free surface which affects  $\sigma_u$  and  $\sigma_w$ , as will be studied in Sect. IV. Besides,  $\tilde{\sigma}_u$  and  $\tilde{\sigma}_w$  increase linearly in Fig. 5 (except for the largest flow rates) with  $Q_j$ , following  $\tilde{\sigma}_u \approx \tilde{\sigma}_w = aQ_j$ , where  $a = 209 \text{ m}^{-2}$ . By symmetry, we assume that the statistical quantities associated to

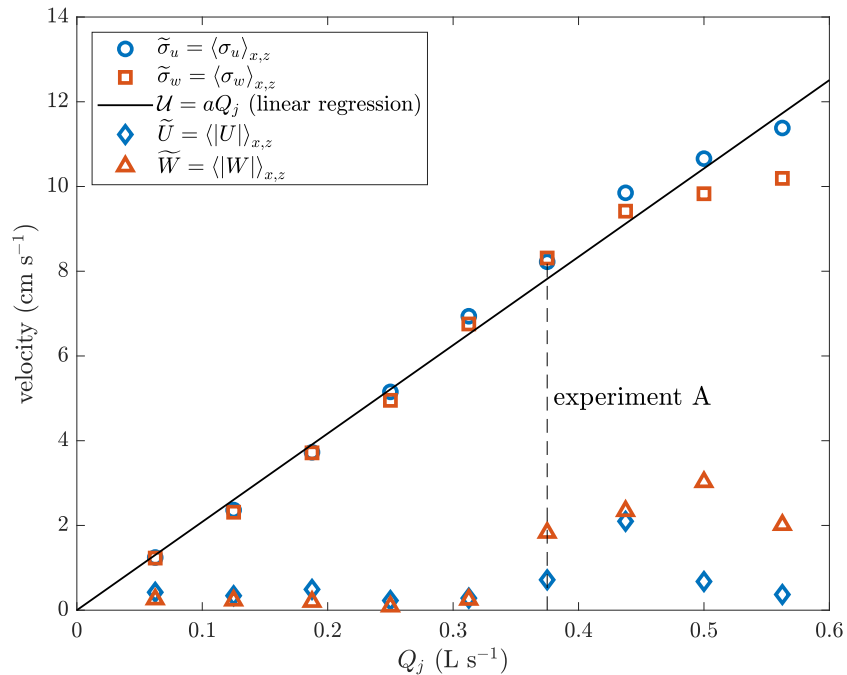


FIG. 5. Standard deviations ( $\tilde{\sigma}_u$  and  $\tilde{\sigma}_w$ ) and mean values ( $\tilde{U}$  and  $\tilde{W}$ ) of horizontal and vertical velocities, averaged over the homogeneous region defined by  $-5 < x < +5$  cm and  $-9 < z < -6$  cm as a function of the flow rate per jet  $Q_j$ . Black line corresponds to the linear regression of equation  $\mathcal{U} = aQ_j$  with  $a = 209 \text{ m}^{-2}$  (95 % CI: [200; 217]), where  $\mathcal{U} = \sqrt{(2\tilde{\sigma}_u^2 + \tilde{\sigma}_w^2)/3}$ .

Flow rate per jet $Q_j$ (L s <sup>-1</sup> )	0.0625	0.125	0.1875	0.25	0.3125	<b>0.375</b>	0.4375	0.5	0.5625
Horizontal velocity fluctuations $\tilde{\sigma}_u$ (cm s <sup>-1</sup> )	1.24	2.36	3.73	5.15	6.94	<b>8.22</b>	9.85	10.66	11.38
Vertical velocity fluctuations $\tilde{\sigma}_w$ (cm s <sup>-1</sup> )	1.23	2.31	3.71	4.95	6.76	<b>8.31</b>	9.42	9.83	10.19
Velocity fluctuations $\mathcal{U} = \sqrt{(2\tilde{\sigma}_u^2 + \tilde{\sigma}_w^2)/3}$ (cm s <sup>-1</sup> )	1.24	2.35	3.72	5.09	6.88	<b>8.25</b>	9.71	10.39	11.00

TABLE I. Parameters and velocity fluctuations of the experiments presented in the paper. Spatial averaging is performed far from the free surface in the homogeneous region defined by  $-5 < x < +5$  cm and  $-9 < z < -6$  cm. Experiment A is in bold.

$v$  are identical to those measured for  $u$ . Thereafter, the turbulence intensity will be characterized by the 3D mean value  $\mathcal{U} = \sqrt{(2\tilde{\sigma}_u^2 + \tilde{\sigma}_w^2)/3}$  [45].  $\mathcal{U}$  is directly related to the turbulent kinetic energy which is equal to  $\mathcal{U}^2/2$ . We also observe in Fig. 5 that mean flow velocities  $\tilde{U} = \langle |U| \rangle_{x,z}$  and  $\tilde{W} = \langle |W| \rangle_{x,z}$ , averaged over the homogeneous region, keep quite low values, remaining at least 3 times smaller than standard deviation values. If we consider that the 1-Hz acquisition rate ensures independence of individual velocity values, confidence intervals (CI) can be evaluated. Using the bootstrap method, we find that the widths of 95 % CI for standard deviations and means are equal to 7 % and 9 % of  $\mathcal{U}$ , respectively. Inspired by the RASJA experiment from [45], our setup thus adds the ability to control the turbulence intensity by replacing the 64 fixed-flow pumps with a variable-flow pump and 64 solenoid valves.

### III. HOMOGENEOUS AND ISOTROPIC TURBULENCE FAR FROM THE FREE SURFACE

In this section, we characterize the turbulent flow far from the free surface (depth  $-9 < z < -6$  cm), i.e., in the part of the homogeneous region belonging to the PIV measurement domain. In this region, the effect of the free surface is negligible and the turbulence is homogeneous and isotropic, as shown in the previous section. The general features of the generated turbulent flows are summarized in Table II and compared to the RASJA experiment of Variano and Cowen [45]. The definitions of characteristic numbers and the methods of calculation are then provided in this section.

	Range of study	Experiment A	Variano and Cowen [45]
Flow rate per jet $Q_j$ (L s <sup>-1</sup> )	[0.06; 0.56]	0.375	0.38
Horizontal velocity fluctuations $\tilde{\sigma}_u$ (cm s <sup>-1</sup> )	[1.24; 11.4]	8.22	3.91
Vertical velocity fluctuations $\tilde{\sigma}_w$ (cm s <sup>-1</sup> )	[1.23; 10.2]	8.31	4.98
Velocity fluctuations $\mathcal{U} = \sqrt{(2\tilde{\sigma}_u^2 + \tilde{\sigma}_w^2)/3}$ (cm s <sup>-1</sup> )	[1.24; 11.0]	8.25	4.30
Anisotropy ratio $\tilde{\sigma}_w/\tilde{\sigma}_u$	[0.90; 1.01]	1.01	1.27
Horizontal fluctuation rate $\tilde{U}/\tilde{\sigma}_u$	[0.032; 0.34]	0.087	0.07
Vertical fluctuation rate $\tilde{W}/\tilde{\sigma}_w$	[0.018; 0.31]	0.22	0.02
Longitudinal horizontal integral length scale $\tilde{L}_{uu}$ (cm)	[6.9; 9.5] (mean: 8.2)	8.4	7.57
Transverse vertical integral length scale $\tilde{L}_{ww}$ (cm)	[3.6; 4.4] (mean: 3.9)	4.2	6.36
Integral length scale ratio $\tilde{L}_{uu}/\tilde{L}_{ww}$ (cm)	[1.9; 2.4] (mean: 2.1)	2.0	1.19
Dissipation rate $\epsilon$ (cm <sup>2</sup> s <sup>-3</sup> )	[0.16; 71]	33	5.20
Kolmogorov length scale $\eta_K$ (mm)	[0.11; 0.50]	0.13	0.21
Kolmogorov time scale $\tau_\eta$ (ms)	[11.9; 250]	17.5	44
Kolmogorov velocity scale $v_\eta$ (mm s <sup>-1</sup> )	[2.0; 9.2]	7.6	4.8
Turbulent Reynolds number $Re_T$	[991; 8801]	6603	3250
Taylor Reynolds number $Re_\lambda$	[148; 558]	461	314

TABLE II. Features of the turbulence in the homogeneous region generated with our RASJA device. First column: range of values measured in this study. Second column: values in the typical experiment A. Third column: values obtained with RASJA experiment by Variano and Cowen [45], presented for comparison.

### A. Integral length scales

Integral length scales characterize the size of the largest eddies and may be computed by the integral of the spatial autocorrelation function for velocities [3]. A relevant integral length scale here is the one involving  $u$  along the longitudinal axis  $O_x$ , for  $y = 0$ . The corresponding normalized autocorrelation function and averaged over time is [3]:

$$\rho_{uu}(r_x, z) = \left[ \frac{\langle u(x, t)u(x + r_x, t) \rangle_x}{\langle u(x, t) \rangle_x^2} \right] \quad (1)$$

where spatial increment  $r_x$  is aligned with  $Ox$ . The longitudinal integral length scale for the horizontal velocity is  $L_{uu}(z) = \int_0^\infty \rho_{uu}(r_x, z) dr_x$ . In the region far from the free surface, we define the normalized autocorrelation function  $\tilde{\rho}_{uu}(r_x) = \langle \rho_{uu}(r_x, z) \rangle_z$ , averaged over vertical space ( $-9 < z < -6$  cm), and its associated integral length scale  $\tilde{L}_{uu} = \int_0^\infty \tilde{\rho}_{uu}(r_x) dr_x$ . The transverse autocorrelation function for the vertical velocity  $\rho_{ww}(r_x, z)$  and its corresponding quantities are defined in the same way by replacing  $u$  by  $w$  in the above equations.  $\tilde{\rho}_{uu}$  and  $\tilde{\rho}_{ww}$  are represented in Fig. 6 (a).

In the homogeneous and isotropic region, we expect to have [3]:

$$\tilde{\rho}_{ww} = \tilde{\rho}_{uu} + \frac{1}{2} r \tilde{\rho}'_{uu} \quad (2)$$

The right part of Eq. (2) is plotted as a red dash-dotted line in Fig. 6 (a) and shows a quite satisfying agreement with  $\tilde{\rho}_{ww}$  (red solid line). Johnson and Cowen [49] performed an exponential fit of  $\tilde{\rho}_{uu}$  and used Eq. (2) to deduce a model for  $\tilde{\rho}_{ww}$ . Here we will do the reverse. Indeed, we observe over all our experiments that  $\tilde{\rho}_{ww}$  (instead of  $\tilde{\rho}_{uu}$  in [49]) can be very well approximated by an exponential fit  $e^{-r_x/\tilde{L}_{ww}}$  for  $r_x < 15$  cm [black dash-dotted line in Fig. 6 (a)]. From Eq. (2), we find that  $\tilde{\rho}_{uu}$  should then be in the form:

$$\tilde{\rho}_{uu} = \mathcal{F}(r_x/\tilde{L}_{uu}) = \frac{1 - e^{-2r_x/\tilde{L}_{uu}}}{2(r_x/\tilde{L}_{uu})^2} - \frac{e^{-2r_x/\tilde{L}_{uu}}}{r_x/\tilde{L}_{uu}} \quad (3)$$

where, theoretically,  $\tilde{L}_{uu} = 2\tilde{L}_{ww}$ . With now  $\tilde{L}_{uu}$  a free parameter, the black dashed line in Fig. 6 (a) fits  $\tilde{\rho}_{uu}$  quite well for  $r_x < 15$  cm with this equation.

At large  $r_x$ , we observe  $w$ -anticorrelation ( $\tilde{\rho}_{ww} < 0$ ) while  $\tilde{\rho}_{uu}$  is above the fitting curve. This is observed in all our experiments for various levels of turbulence (not shown here). This may be explained by large-scale currents in the experiment.



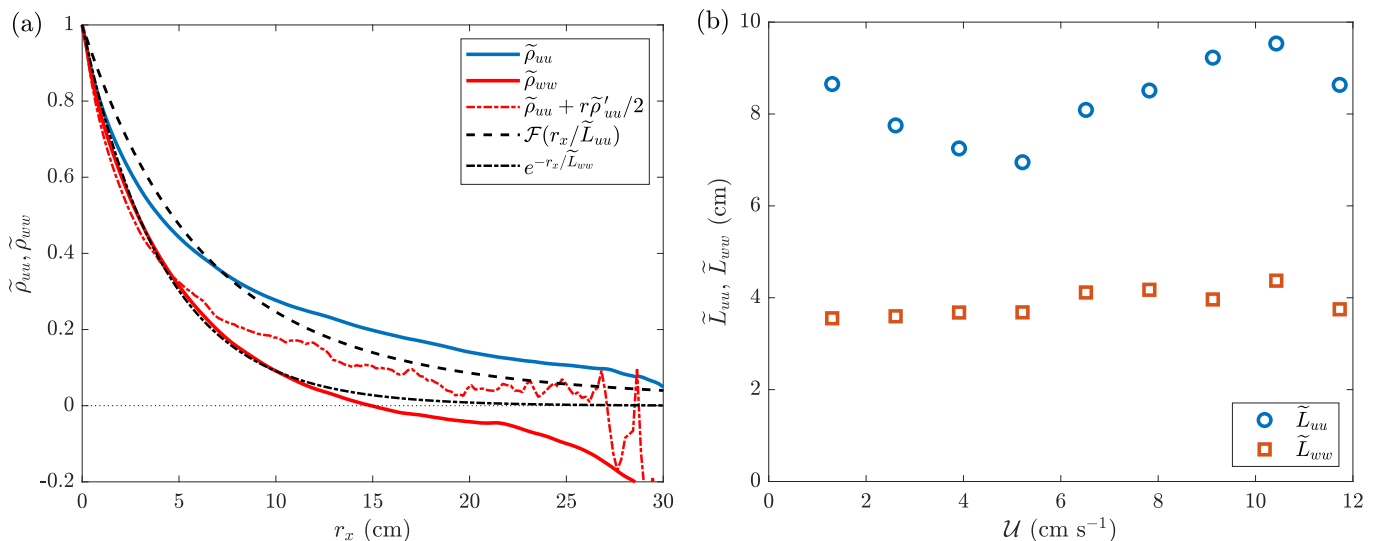


FIG. 6. (a) Autocorrelation functions  $\tilde{\rho}_{uu}$  and  $\tilde{\rho}_{ww}$  (blue and red solid lines, respectively) of horizontal and vertical velocities  $u$  and  $w$  along  $x$  as functions of spatial increment  $r_x$ .  $\tilde{\rho}_{ww}$  obtained from Eq. (2) is also displayed (red dash-dotted line), as well as curve fitting (black dashed line representing  $\tilde{\rho}_{uu}$  from Eq. (3) and black dash-dotted line being an exponential fit of  $\tilde{\rho}_{ww}$ ). Parameters of Experiment A;  $y = 0$  and averaged over  $z \in [-7; -6]$  cm (full-width illuminated region). (b) Longitudinal  $\tilde{L}_{uu}$  and transverse  $\tilde{L}_{ww}$  integral scales of horizontal and vertical velocities respectively versus velocity fluctuations  $U$ . Integral scales are obtained by integration over  $r_x$  of curves fitting  $\tilde{\rho}_{uu}$  and  $\tilde{\rho}_{ww}$  as shown in (a).

Figure 6 (b) displays the fitting parameters  $\tilde{L}_{uu}$  and  $\tilde{L}_{ww}$  as a function of  $U$  and shows that they are quite independent of the turbulence intensity. On average, we find  $\tilde{L}_{uu} = 8.3$  cm and  $\tilde{L}_{ww} = 3.9$  cm, so  $\tilde{L}_{uu}/\tilde{L}_{ww}$  is 2.1 on average, which is very close to the theoretical ratio of 2 in the case of homogeneous and isotropic turbulence. For comparison, Variano and Cowen [45] found a ratio  $\tilde{L}_{uu}/\tilde{L}_{ww} = 1.19$ . Thereafter,  $L = \tilde{L}_{uu} \approx 8$  cm characterizes the size of the largest eddies and is used as the integral length scale of the flow.

## B. Dissipation rate

The dissipation rate  $\epsilon$  is associated with the energy injected at large scales, which goes through inertial scales and is finally dissipated at small scales. It is defined by  $\epsilon = 2\nu \langle S_{ij} S_{ij} \rangle$ , where  $S_{ij} = (\partial u_i / \partial x_j + \partial u_j / \partial x_i) / 2$  is the velocity gradient and  $\nu = 1 \cdot 10^{-6} \text{m}^2 \text{s}^{-1}$  the kinematic viscosity of water. Our PIV resolution is not large enough to compute  $\epsilon$  from this definition. But it can be computed through time-averaged second-order structure functions along  $x$  [3]:

$$D_{LL}(r_x) = \overline{\langle [u(x, t) - u(x + r_x, t)]^2 \rangle_x} \quad (4)$$

$$D_{NN}(r_x) = \overline{\langle [w(x, t) - w(x + r_x, t)]^2 \rangle_x} \quad (5)$$

where  $r_x$  is the spatial increment along  $Ox$  axis. In the inertial range,  $D_{LL} = C_2(\epsilon r_x)^{2/3}$  and  $D_{NN} = \frac{4}{3}C_2(\epsilon r_x)^{2/3}$ , with  $C_2 = 2.0$  [3]. We computed the associated dissipation rate  $\epsilon_{D_{LL}}$  and  $\epsilon_{D_{NN}}$  for various  $r_x$ . The obtained values display a good homogeneity over the whole inertial range as shown in Fig. 7. By averaging them over the interval  $2 < r_x < 6$  cm, we obtain the estimations for dissipation rate  $\tilde{\epsilon}_{D_{LL}}$  and  $\tilde{\epsilon}_{D_{NN}}$ , which have similar values and are plotted in Fig. 8 as functions of  $U^3$ . The linear shape of the curve is compatible with the scaling law  $\epsilon = AU^3/L$ , with  $A = 0.42$ . The value of  $A$  is of the same order of magnitude of the one found by Variano and Cowen [45] ( $A \approx 0.52$ ). In the following, the dissipation rate is  $\epsilon = (\tilde{\epsilon}_{D_{LL}} + \tilde{\epsilon}_{D_{NN}}) / 2 \in [0.16; 71] \text{cm}^2 \text{s}^{-3}$ .

These values of  $\epsilon$  give us access to Kolmogorov length, time and velocity scales,  $\eta_K = (\nu^3/\epsilon)^{1/4} \in [0.11; 0.50]$  mm,  $\tau_\eta = (\nu/\epsilon)^{1/2} \in [11.9; 250]$  ms and  $v_\eta = (\nu\epsilon)^{1/4} \in [2.0; 9.2]$  mm.s<sup>-1</sup>, which are characteristic scales of the smallest turbulent motions [3].

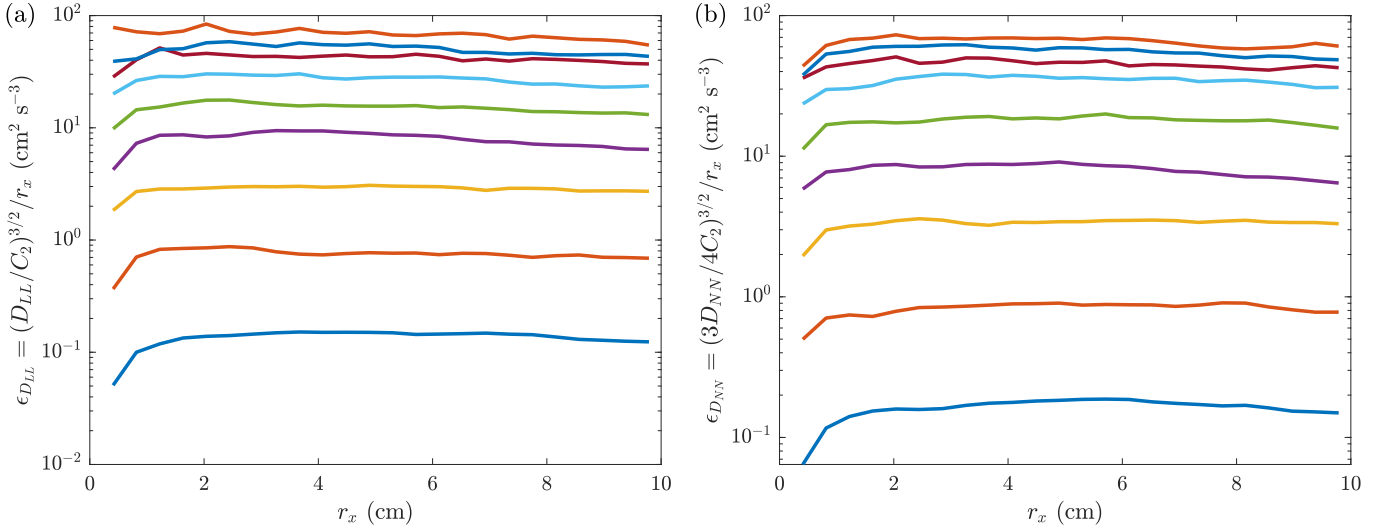


FIG. 7. Dissipation rates  $\epsilon_{D_{LL}}$  and  $\epsilon_{D_{NN}}$  computed from longitudinal and transverse second-order structure functions (a)  $D_{LL}$  for horizontal velocity  $u$  and (b)  $D_{NN}$  for vertical velocity  $w$  as functions of the spatial increment  $r_x$ . Lines of increasing mean values correspond to increasing levels of turbulence,  $\mathcal{U}$ .  $y = 0$ ,  $z = -6.4$  cm.

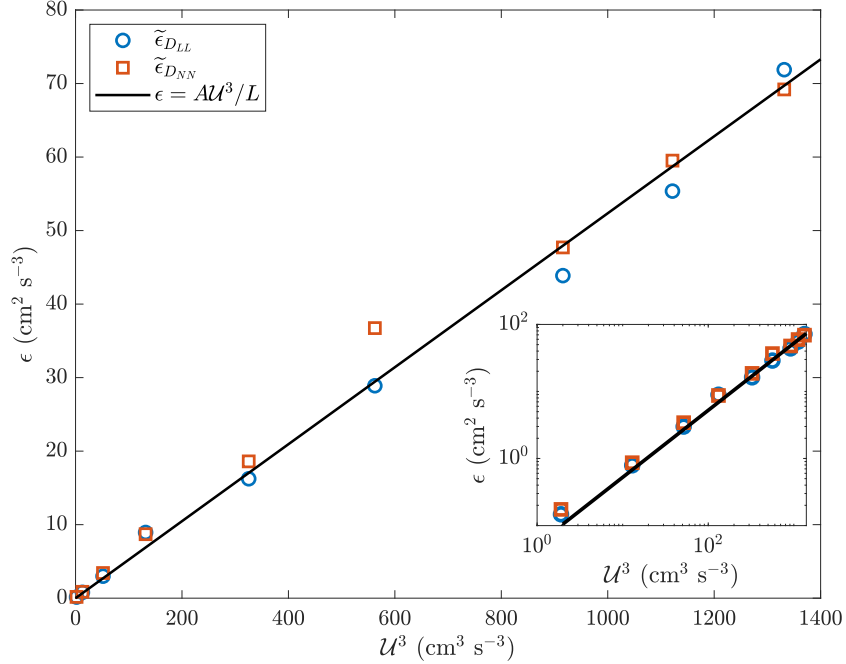


FIG. 8. Estimations of dissipation rates  $\tilde{\epsilon}_{D_{LL}}$  and  $\tilde{\epsilon}_{D_{TT}}$  as functions of turbulent velocity fluctuations  $\mathcal{U}^3$ , obtained by averaging over spatial increment  $r_x$  dissipation rates plotted in Fig. 7. Solid line corresponds to the scaling law  $\epsilon = A\mathcal{U}^3/L$ , with  $A = 0.42$  (95% CI: [0.41; 0.43]) and  $L = 8$  cm. Inset: same as the main plot but in logarithmic scale.

### C. Velocity power spectra

Homogeneous and isotropic turbulence is a scale-invariant phenomenon, which is thus well described in the spatial Fourier space. The power-law behavior of the one-dimensional velocity power spectrum  $S(k) = C \epsilon^{2/3} k^{-5/3}$  in the inertial range (predicted by Kolmogorov in 1941) constitutes one of the most robust results in homogeneous and isotropic turbulence [2–4, 58].  $k$  is the spatial wavenumber and  $C \approx 1.5$  is the experimentally measured Kolmogorov constant [3, 59]. Normalized spatial power spectra of turbulent velocity fluctuations are computed along the horizontal coordinate  $x$  for  $u$  and  $w$  on instantaneous velocity fields multiplied by Blackman–Harris window functions.

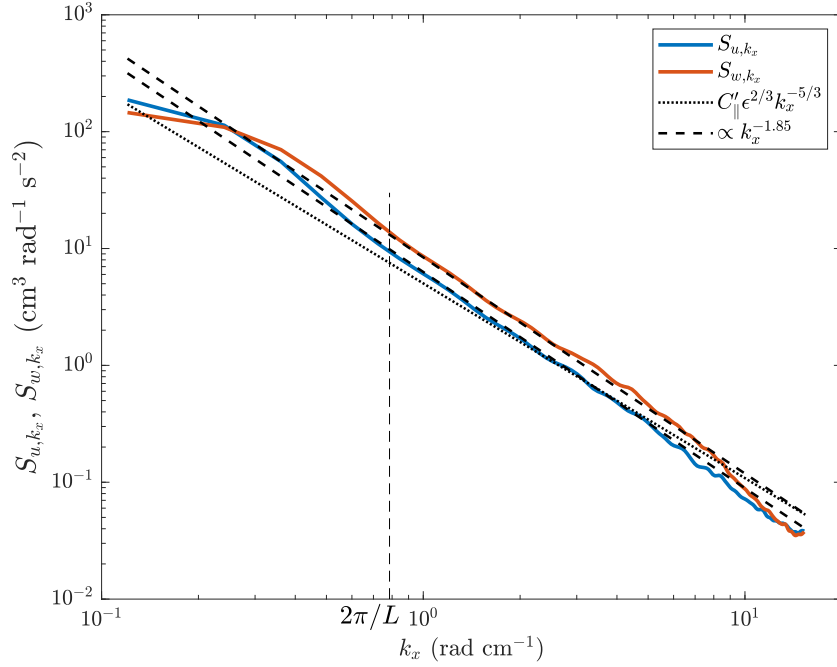


FIG. 9. Longitudinal (blue) and transverse (red) spatial power spectra of horizontal and vertical turbulent velocity fluctuations  $S_{u,k_x}$  and  $S_{w,k_x}$  along  $x$  as functions of horizontal wavenumber  $k_x$  far from the free surface and averaged over time. Dotted line represents the theoretical longitudinal spectra  $C'_{\parallel} \epsilon^{2/3} k_x^{-5/3}$ . Dashed lines correspond to the scaling law  $k_x^{-1.85}$  and differ from each other by a factor  $C'_{\perp}/C'_{\parallel} = 4/3$ . Parameters of Experiment A;  $y = 0$  and  $z = -6.4$  cm.

The squared modulus of the fast Fourier transform is normalized and averaged over time, yielding longitudinal and transverse spectra,  $S_{u,k_x}$  and  $S_{w,k_x}$ , displayed in Fig. 9 for  $z = -6.4$  cm.

Due to isotropy, the  $\epsilon^{2/3} k^{-5/3}$  power law is also expected in the sub inertial range for  $S_{u,k_x}$  and  $S_{w,k_x}$  but with different dimensionless prefactors,  $C'_{\parallel} = 18/55 C$  and  $C'_{\perp} = 24/55 C$  for the longitudinal and transverse spectra, respectively [3]. The black dotted line in Fig. 9 denotes the longitudinal theoretical Kolmogorov 41 power-law spectrum  $C'_{\parallel} \epsilon^{2/3} k_x^{-5/3}$ , using  $\epsilon$  from Sect. III B and showing a rough agreement with the experimental longitudinal spectrum (blue line). Indeed, experimental spatial spectra show a slightly steeper scaling law ( $\propto k_x^{-1.85}$ , represented by dashed lines), as observed in the experiment of Variano and Cowen [45]. The relative position of observed longitudinal and transverse spectra is consistent with the hypothesis of homogeneous and isotropic turbulence [3]:  $S_{u,k_x} < S_{w,k_x}$  in the inertial range while  $S_{u,k_x} > S_{w,k_x}$ , for the smallest wavenumbers. According to the Kolmogorov 41 power spectrum,  $S_{w,k_x}/S_{u,k_x} = C'_{\perp}/C'_{\parallel} = 4/3$  in the inertial range [3]. Figure 9 shows that this ratio is verified experimentally as the longitudinal fit multiplied by  $4/3$  fits well the transverse spectrum.

The temporal velocity power spectra are displayed in Fig. 10, obtained from LDV measurements for  $z = -6.6$  cm and for experimental parameters close to those of Experiment A. We observe a  $\omega^{-5/3}$  power-law spectrum in the inertial range for  $u$  and  $w$  for  $\omega \in [2, 50]$  rad s $^{-1}$ . This power-law spectrum is theoretically predicted using the random sweeping model of Tennekes [58] and is derived from the Kolmogorov 41 spectrum in space ( $\sim k_x^{-5/3}$ ). The physical origin is similar to Taylor's frozen turbulence hypothesis, valid in the case of turbulence with a mean flow. Here, in the absence of a global mean flow, the scaling law is explained by the advection of the small eddies (inertial range) and of their spatial structure by the largest eddies. Temporal fluctuations in the corresponding frequencies are thus similar to spatial fluctuations. Tennekes thus predicts that the spectral density is  $S_{u,\omega} = S_{w,\omega} = \beta_E (\sqrt{3} U \epsilon)^{2/3} \omega^{-5/3}$ , with  $\beta_E \sim 1$ . In Fig. 10, by using the relation  $\epsilon = AU^3/L$  determined from Fig. 8 and by choosing  $\beta_E = 0.7$ , we find that this theoretical equation fits very well to our data. We note that the vertical velocity spectrum  $S_{u,\omega}$  displays a peak around  $\omega = 40 - 50$  rad s $^{-1}$ , probably due to mechanical oscillations of the setup, this frequency being quite independent of forcing. However, our setup is not excited at particular frequencies other than this one, contrary to oscillating-grid turbulence experiments. Thus, the inertial range of our temporal spectra in Fig. 10 is not polluted by numerous peaks due to the oscillation frequency of a grid and its harmonics [33, 37].

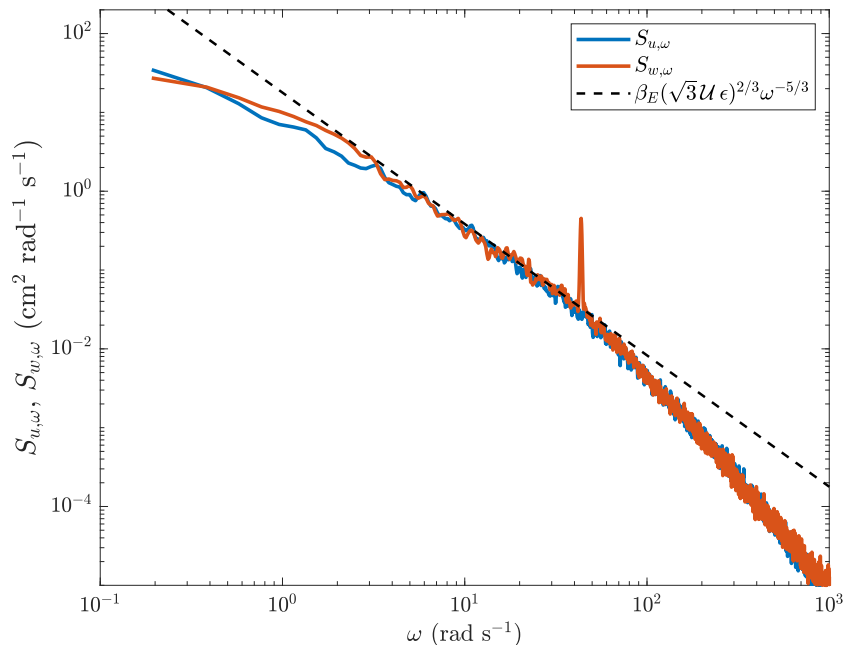


FIG. 10. Temporal power spectra  $S_{u,\omega}$  and  $S_{w,\omega}$  of the horizontal (blue) and vertical (red) velocity as functions of the angular frequency  $\omega$  for  $x = 0$ ,  $y = -7$  cm and  $z = -6.6$  cm with two distinct LDV measurements for horizontal and vertical velocities  $u$  and  $w$ . Dashed line represents the theoretical law predicted by Tennekes [58] choosing  $\beta_E = 0.7$ . Duration: 1200 s.  $Q_j = 0.25$  L  $s^{-1}$ .  $U = 6.1$  cm  $s^{-1}$ .

#### D. Reynolds numbers

The level of turbulence reached within our experimental device is quantified by computing two common Reynolds numbers of the flow: the turbulent Reynolds number  $Re_T = UL/\nu$  associated with the integral length scale and the large-scale velocity fluctuations, and the Taylor-scale Reynolds number  $Re_\lambda = U^2 \sqrt{15/(\nu\epsilon)}$  linked to the typical size of velocity gradients and characterizing the turbulent cascade [3, 4]. The variables estimated in the previous subsections are then used to compute the corresponding values of these two Reynolds numbers, to compare the performances of our experimental device with other RASJA or grid-stirred tank experiments. For our range of flow rates, we obtain  $Re_T$  between 991 and 8801 and  $Re_\lambda$  between 148 and 558. We find  $20Re_T/Re_\lambda^2 \in [0.53; 0.90]$ , which is compatible with theory predicting  $Re_T \sim Re_\lambda^2/20$  [3]. The largest values are significantly greater than the ones obtained with the RASJA of Variano and Cowen [45], where the maximal values are  $Re_\lambda = 314$  and  $Re_T = 3220$ , with 64 bilge pumps located at the bottom of a tank ( $80 \times 80 \times 100$  cm) with a free surface. We note that two recent RASJA experiments with two vertical opposing walls of jets have reached slightly larger values:  $Re_\lambda = 496$  in air with 256 jets by Carter *et al.* [48, 60] and  $Re_\lambda = 587$  in water with 96 jets by Esteban *et al.* [50], but this configuration of jets is not adapted to the interaction of turbulence with a free surface. In contrast, the previous experimental devices studying turbulence at the vicinity of the free surface are mostly grid-stirred tanks [8, 33, 36, 37], for which the level of turbulence is significantly smaller, with  $Re_\lambda < 100$  and  $Re_T < 500$  [61].

To conclude this section, we demonstrate that our original experimental device associating a large pump with randomly opened jets constitutes a convenient facility to study homogeneous and isotropic turbulence with low mean flow and circulation and with a sufficient Taylor-scale Reynolds number to obtain a developed inertial range. The temporal velocity power spectrum in Fig. 10 thus displays a power-law in  $\omega^{-5/3}$  on more than one decade and the ratio between the longitudinal integral length and the Kolmogorov scale reaches values in the order of 500. Moreover, by increasing the flow rate of the central pump, the turbulent Reynolds number can be varied, while keeping the longitudinal integral length around 8 cm, with good levels of isotropy and homogeneity and with low mean flow. We note also that we can reach higher values of the dissipation rate (with a maximal value of  $\epsilon = 71$  cm<sup>2</sup> s<sup>-3</sup>) than in the other RASJA experiments (which are typically twice larger in width), where the maximal value of  $\epsilon$  is of order 5 cm<sup>2</sup> s<sup>-3</sup> in the experiment of Variano and Cowen [45], 15 cm<sup>2</sup> s<sup>-3</sup> in the experiment of Esteban *et al.* [50] and 36 cm<sup>2</sup> s<sup>-3</sup> in the experiment of Johnson and Cowen [49]. Levels of dissipation rate equivalent to ours or higher, using water as a fluid, can only be reached in closed tanks, where the turbulence is driven by the rotation of propellers [62] or impellers like Von-Kármán swirling flows [63], but they are not suitable to study a free surface. Finally, we note

that our device has been explored only for a specific configuration of the jet patterns, opening duration, and water-filling depth. Numerous flow configurations could be tested and used in further research in fundamental or applied turbulence.

#### IV. TURBULENCE ANISOTROPY NEAR THE FREE SURFACE

In this section, we study the turbulent flow in the region where the free surface makes turbulence anisotropic, i.e., for  $-6 < z < 0$  cm. As reported in previous studies [33, 45], the vertical size of this domain is of order the longitudinal integral scale. While the measurement of the free-surface deformation and the subsequent analysis will be reported in further dedicated work, we must note that the rms amplitude of the free-surface deformation  $\sigma_\eta$  does not exceed 2 mm for the range of turbulence level studied here [56]. By assimilating the integral scale  $L = \tilde{L}_{uu} \approx 8$  cm as the size of the free-surface excitation by the flow, the ranges of the Froude number  $\text{Fr} = U/\sqrt{2gL}$  and Weber number  $\text{We} = (\rho U^2 L)/(2\gamma)$ , built on the integral scale [5], are respectively [0.010; 0.088] and [0.088; 6.9], where  $g = 9.81$  m s<sup>-2</sup> is the gravity acceleration,  $\rho = 998$  kg m<sup>-3</sup> the water density and  $\gamma \approx 0.07$  N m<sup>-1</sup> the air-water surface tension. According to the qualitative analysis of free-surface deformations in the presence of turbulence by Brocchini and Peregrine [5], given the intensity of turbulence ( $U \in [1.24; 11.0]$  cm s<sup>-1</sup>) with  $L \approx 8$  cm, our experiments belong to the "flat" or the "wavy" domain. For these parameters, the "wavy" domain indeed starts at  $U \approx 2.8$  cm s<sup>-1</sup> and the breaking transition occurs for  $U \approx 32$  cm s<sup>-1</sup> [5]. Consequently, a breaking of the free surface is not expected and not observed for these levels of turbulence. As the deformations remain small compared to the integral length  $L$ , the free-surface dynamics is expected to act as a free-slip rigid surface in first approximation [5]. We note, that in the case of significant surface deformations, the velocity field characterization using PIV would require the simultaneous measurement of the free surface shape to apply the PIV algorithms only in the liquid domain. Such a challenging experimental implementation has not yet been performed for a free surface deformed by the turbulence and is limited to two-dimensional [64] or axisymmetric [65] flows and interface deformations.

##### A. Velocity fluctuations near the free surface

We use the PIV measurements to investigate the influence of the free surface on the turbulent velocity field for  $-6 < z < 0$  cm. In Fig. 2, the influence of the top free surface becomes clearly visible for  $z > -4$  cm. We note that the vertical fluctuations  $\sigma_w$  show a good level of homogeneity along the horizontal coordinate  $x$ , whereas  $\sigma_u$  is maximal at the tank center and significantly decreases on the sides of the images as visible in Fig. 3 (b). This behavior is likely due to the finite-size effects of the tank as stated by Variano and Cowen [45]. The main effect of the free surface is displayed by the vertical dependency of velocity fluctuations. The strong modification of velocity fluctuations shown in Fig. 2 is highlighted when averaging horizontally the vertical profiles of velocity as plotted in Fig. 11 (a):  $\sigma_w$  is found to decrease close to the free surface while  $\sigma_u$  increases except over a 1-cm-thick layer just beneath the free surface. While we observe good isotropy for  $z < -6$  cm, the turbulent flow thus becomes strongly anisotropic near the free surface ( $z = 0$ ). This increase of the flow anisotropy when approaching the free surface is also reported in the experimental work of Variano and Cowen [45] and in the experiments performed with grid stirred tanks [33, 37]. In these studies like ours, the turbulent flow becomes affected by the free surface for depth of order or smaller than the integral length  $L$ .

The increase of turbulence anisotropy when approaching a wall has been addressed theoretically first by Hunt and Graham [28, 66]. Using the rapid distortion theory (RDT), they consider the displacement of a turbulent structure from the homogeneous isotropic region towards the interface and compute as a potential flow the modification of the structure in a linear framework without dissipation. The free surface plays the role of a rigid wall limiting vertical motions of the fluid. Then a transfer from vertical kinetic energy to horizontal kinetic energy occurs. The affected depth depends on the typical size of the largest eddies  $L$ . Indeed, Hunt [66] predicts for shear-free turbulence that the vertical velocity fluctuations near a horizontal wall scale as  $\sigma_w \propto |z|^{1/3}$  in a layer defined by  $-L \lesssim z \leq 0$ , except in a viscous boundary layer close to the wall. Using numerical simulations, Calmet and Magnaudet investigate specifically the case of a free surface modeled as a free-slip rigid wall [19]. They find a thickness of the viscous layer of order  $\delta_\nu \approx 2.0 L/\sqrt{2\text{Re}_T}$  in agreement with previous experimental measurements [33]. This formula gives  $\delta_\nu \in [1.7; 5.1]$  mm for our experiments where the largest values correspond to the lowest turbulent intensities. By taking into account this viscous boundary layer, they predict the following evolution of the vertical velocity fluctuations for  $-L \lesssim z \leq \delta_\nu$ :

$$\sigma_w = \sqrt{\beta}\epsilon^{1/3} \left( \frac{L(|z| - \delta_\nu)}{L - \delta_\nu} \right)^{1/3} \quad (6)$$

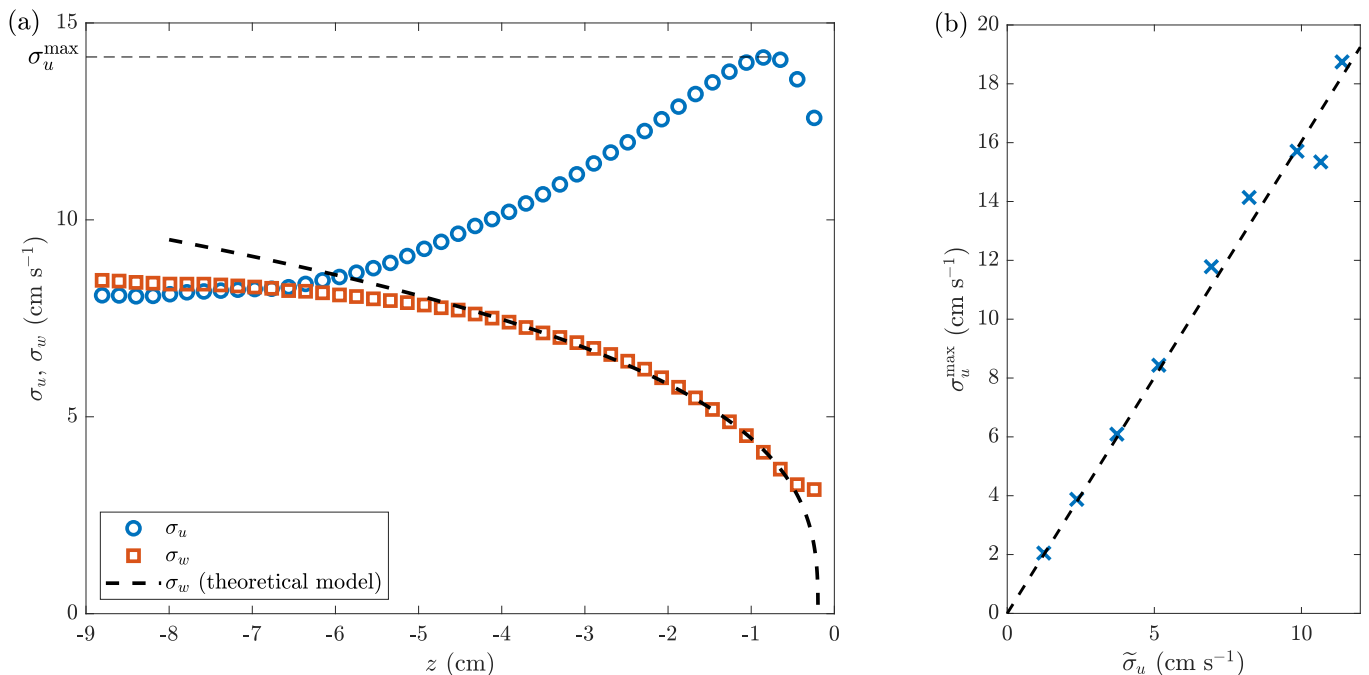


FIG. 11. (a) Vertical profiles of standard deviations for horizontal and vertical velocities  $\sigma_u$  and  $\sigma_w$ , averaged horizontally over  $-5 < x < +5$  cm. Theoretical model (dashed line) corresponds to Eq. (6) with  $L = 8$  cm,  $\beta = 2.2$ . The evolution of vertical fluctuations as a function of the distance to the free surface  $z$  is well described by this model for  $z < 0.6L \approx 4.8$  cm. Parameters of Experiment A. (b) Maximum of  $\sigma_u$  from (a) as a function of its value in the homogeneous and isotropic region,  $\tilde{\sigma}_u$ . Dashed line corresponds to a linear regression:  $\sigma_u^{\max}/\tilde{\sigma}_u = 1.60$  (95% CI: [1.52; 1.68]).

where the prefactor  $\beta$  is theoretically computed to be  $\beta = 1.784$  [30]. In stationary regime, this expression of  $\sigma_w$  has been verified for  $-0.7L \lesssim z \lesssim \delta_\nu$  in numerical simulations [19] by choosing  $\beta \approx 2.0$ . Variano and Cowen [45] experimentally measured  $\beta \approx 1.5$  and observed that the model is valid for  $z > -L$ , the viscous layer being unresolved.

In Fig. 11 (a), we add the curve corresponding to Eq. (6), which fits well with the experimental profile of vertical velocity fluctuations  $\sigma_w$  for  $-0.6L \leq z \leq 0$  when choosing  $\beta = 2.2$  and the parameters  $L$ ,  $\epsilon$  and  $\text{Re}_T$  characterizing the turbulence in the bulk, determined in Sect. III. For the other flow rates (not shown), we find again a good agreement between the theoretical vertical fluctuation profile and experimental profile in the domain  $-0.6L \leq z \leq 0$  for our range of  $\text{Re}_T$  by choosing  $2.0 \lesssim \beta \lesssim 2.3$ .

Notice that the decrease of  $\sigma_w$  slows down very close to the free surface [for  $z > -0.5$  cm in Fig. 11 (a)]. This departure from the theoretical curve can be detected only for an intense enough turbulence ( $\mathcal{U} \gtrsim 5$   $\text{cm s}^{-1}$  or  $\text{Re}_T \gtrsim 3000$ ). Moreover, the depth of this inflection point increases with forcing while  $\delta_\nu$  decreases, implying that this observation is not related to the viscous sublayer. This effect is probably due to the small deformations (few millimeters) of the free surface caused by turbulence. Indeed, this effect is neither visible for the lowest forcings of our experiment nor in Variano *et al.* experiment which displays only gentle free-surface deformation and where  $\sigma_w$  seems to decrease to zero at the free surface. By taking into account the free-surface displacement  $\eta(t)$  [i.e.,  $w(z=0, t) \approx \partial\eta/\partial t$ ], the free surface does not behave anymore as a rigid shear-free wall. Consistently with our measurements, Guo and Shen observe in their numerical simulations a nonvanishing value of  $w$  in  $z=0$  which increases with Froude number and thus with surface deformations [26]. Measurements with better resolution near the free surface are needed to confirm and analyze this observation.

A theoretical prediction similar to Eq. (6) exists for  $\sigma_u$  [30, 66] but was shown to be valid only for  $-0.1L < z < 0$  [19], which is a too small range to be verified in our experimental setup. But the same studies also predicts in first approximation that  $\sigma_u$  should monotonically increase when approaching the free surface and reach  $\sigma_u^2(z=0) = 1.5\tilde{\sigma}_u^2$ , i.e., an increase of 22% for  $\sigma_u$ . As visible in Fig. 11 (a), we do not observe such a monotonic increase in our experiments as  $\sigma_u$  reaches a maximum at  $z \approx -0.9$  cm. The position of this maximum appears to be independent of the forcing (not shown here), contrary to the size  $\delta_\nu$  of the viscous sublayer which is thus not involved. The same phenomenon at a similar vertical location appears in Variano and Cowen [45] experiment. This non-monotonic evolution of  $\sigma_u$  is interpreted by these authors as a contamination of the air-water interface by surfactants, which changes the boundary condition. In the case of a solid wall,  $\sigma_u$  is expected to reach 0 in  $z=0$  due to the no-slip boundary condition. For a free surface, one expects  $du/dz|_{z=0} = 0$  due to the absence of tangential forces, as observed in numerical simulations.

However, a free surface contaminated with surfactants may have a behavior close to a solid wall as surfactants induce horizontal surface tension gradients creating tangential forces called Marangoni stresses [67]. Such pollution of the free surface is very difficult to avoid in experiments using water [68–72]. The influence of surfactants on the mechanical properties of a free surface has been investigated for various levels of contamination in numerical simulations [23, 25], showing a decrease of the value of  $\sigma_u$  at the free surface, but without a nonmonotonic evolution.

Nevertheless, the increase of  $\sigma_u$  with  $z$  before the maximum is consistent with the conversion of vertical fluctuations into horizontal ones. Then, we plot in Fig. 11 (b) the maximum of horizontal velocity fluctuations,  $\sigma_u^{max}$ , as a function of  $\tilde{\sigma}_u$ , the value in the homogeneous and isotropic region. We observe a clear linear relation  $\sigma_u^{max} = 1.6\tilde{\sigma}_u$ . This 60 % increase is much larger than the predicted 22 % by the RDT [28, 30].

Conversely, we can read an increase of only 10 % in figures of Variano and Cowen [9, 45]. Guo and Shen [26] showed in their numerical simulations that this increase greatly depends on surface behavior. It reaches 45 % for the weakest surface deformations ( $Fr = 0.22$  using our definition) and seems to be around 25 % and 20 % for  $Fr = 0.32$  and  $Fr = 0.63$  respectively. Notice that Froude numbers for our experiments are smaller ([0.010; 0.088]) which may explain an even larger increase. Interpretation of this over-amplification relative to the RDT has been proposed by Hunt [66] and Kit *et al.* [73], including nonlinear vortex stretching near the interface, but was discredited by Magnaudet [30]. For our experiment, this result may also be linked to the important horizontal inhomogeneity observed for horizontal velocity fluctuations near the free surface in Fig. 3 (b), which could concentrate the energy in the horizontal center of the tank.

To conclude, our measurements show that the turbulent velocity fluctuations are affected by the top free surface, with an enhancement of the horizontal fluctuations and a decrease of the vertical ones. These observations complete previous experimental [33, 45] and numerical [19, 26] results of the literature and are in qualitative agreement with the predictions of the RDT describing the geometric deformation of a turbulent flow at the vicinity of a rigid surface [28, 30, 66]. However, we observe that near the surface, horizontal velocity fluctuations increase much more than predicted theoretically.

## B. Velocity power spectra near the free surface

The modification of the turbulence at the vicinity of the free surface is also well characterized by the velocity power spectra. In Sec. III C, we show in Fig. 9 that the energy spectra of horizontal and vertical velocities computed far from the free surface are in satisfying agreement with the Kolmogorov 41 predictions for homogeneous and isotropic turbulence. The anisotropy of turbulent fluctuations when we get closer to the free surface, mentioned in Sect. III, is also reflected in the spatial spectra recorded close to the free surface, as shown in Fig. 12 (a) for  $z = -1.1$  cm. At large scale (small horizontal wavenumber  $k_x$ ), the amplitude of the horizontal velocity spectrum  $S_{u,k_x}$  is enhanced, whereas the one of the vertical velocity spectrum  $S_{w,k_x}$  is reduced. This observation is consistent with the conversion of vertical fluctuations into horizontal ones, discussed in Sect. IV A for the profile of horizontal fluctuations.

To have a better grasp of what happens at different scales, we display in Fig. 13, the (a) longitudinal and (b) transverse spatial power spectra at different depths. A transition wavenumber  $k_{u,t} \approx 2\pi/L$ , roughly independent of the depth, appears to separate the longitudinal spectrum into two parts. At small scales ( $k_x > k_{u,t}$ ), we observe the turbulence remains isotropic and satisfyingly follows the same power law in  $k^{-1.85}$  with the same parameters  $C'_{\parallel}$  and  $\epsilon$  as in the homogeneous and isotropic region. At large scales ( $k_x < k_{u,t}$ ), the amplitude of the longitudinal spectrum in Fig. 13 (a) increases when approaching the free surface.

For the transverse spectrum in Fig. 13 (b), the transition between large scales (reduced spectrum amplitude) and small scales (unchanged spectrum) occurs for a wavenumber  $k_{w,t}$  increasing when getting closer to the free surface.  $k_{w,t}$  is defined as the wavenumber for which the large-scale part of  $S_{w,k_x}$  deviates from the  $k_x^{-1.85}$  power law and is below the corresponding dashed line [see Fig. 12 (a) and Fig. 13 (b)]. We plot in Fig. 12 (b) the inverse of  $k_{w,t}$  as a function of the depth. We observe that the transition is linearly linked to the depth for  $z > -6$  cm with  $|z|k_{w,t} \approx 1.4$  rad. This illustrates that the vertical velocity of eddies smaller than  $L$  and larger than the fluid depth is transferred to large-scale horizontal velocity near the free surface.

We complete the PIV measurements, with temporal spectra acquired using LDV at  $z \approx -1$  cm and displayed in Fig. 14. The dashed line corresponds to the Tennekes model in  $\omega^{-5/3}$  with the same  $\beta_E$ ,  $\mathcal{U}$  and  $\epsilon$  values as in Sect. III C and Fig. 10. Then, we observe the velocity fluctuations follow the same equation as in the homogeneous and isotropic region in the mid range of frequencies. In addition, the  $\omega^{-5/3}$  power law is considerably extended towards low frequencies ( $\omega \lesssim 3$  rad s $^{-1}$ ) for the horizontal velocity spectrum  $S_{u,\omega}$ , whereas the large-scale vertical velocity spectrum  $S_{w,\omega}$  is reduced. The fact that the horizontal temporal velocity spectrum scales as  $\omega^{-5/3}$  even for low frequencies while it is not the case of the spatial spectrum in Fig. 13 (a) is surprising as the temporal spectrum is supposed to result from spatial structure advection, according to Tennekes model [58]. Besides, the significant extension towards low frequencies of the Kolmogorov spectrum of horizontal velocity close to a free surface despite

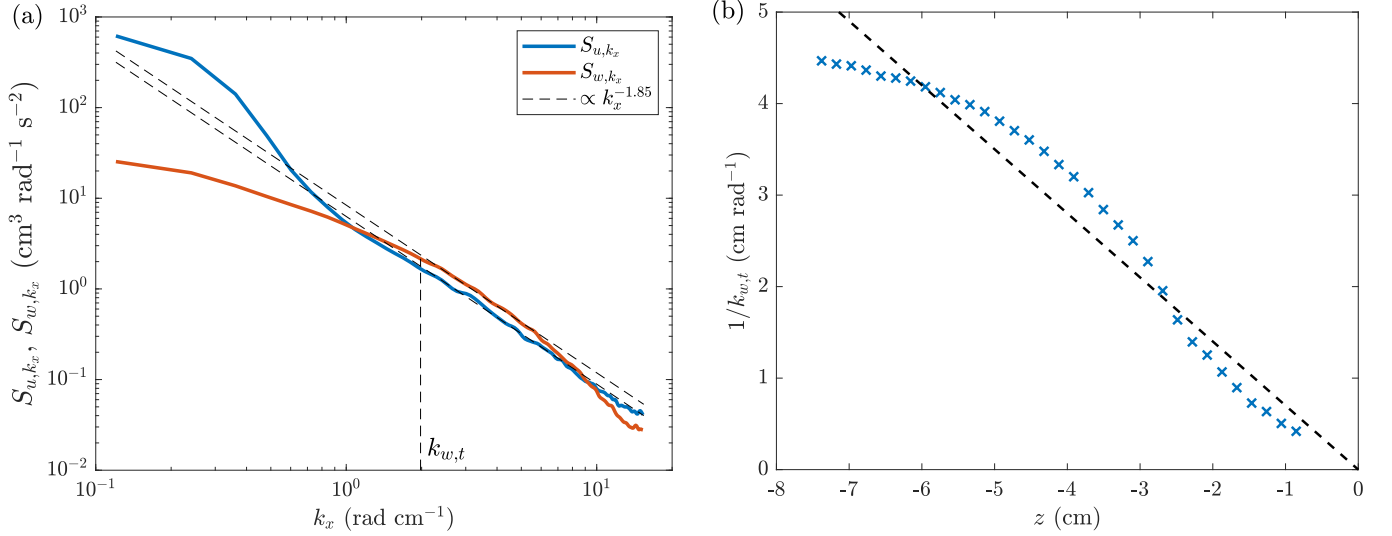


FIG. 12. (a) Longitudinal (blue) and transverse (red) spatial power spectra of horizontal and vertical turbulent velocity fluctuations  $S_{u,k_x}$  and  $S_{w,k_x}$  along  $x$  as functions of horizontal wavenumber  $k_x$  close to the free surface and averaged over time. Dashed lines represent the same power law in  $k_x^{-1.85}$  and the same prefactor as in Fig. 9. Parameters of Experiment A;  $y = 0$  and  $z = -1.1$  cm. (b) Inverse of the wavenumber  $k_{w,t}$  for which  $S_{w,k_x}$  deviates from  $k_x^{-1.85}$  power law [see Figs 12(a) and 13(b)], as a function of depth. Dashed line is a linear fit corresponding to the equation  $z k_{w,t} = -b$ , with  $b = 1.43$  rad (95% CI: [1.38; 1.48] rad).

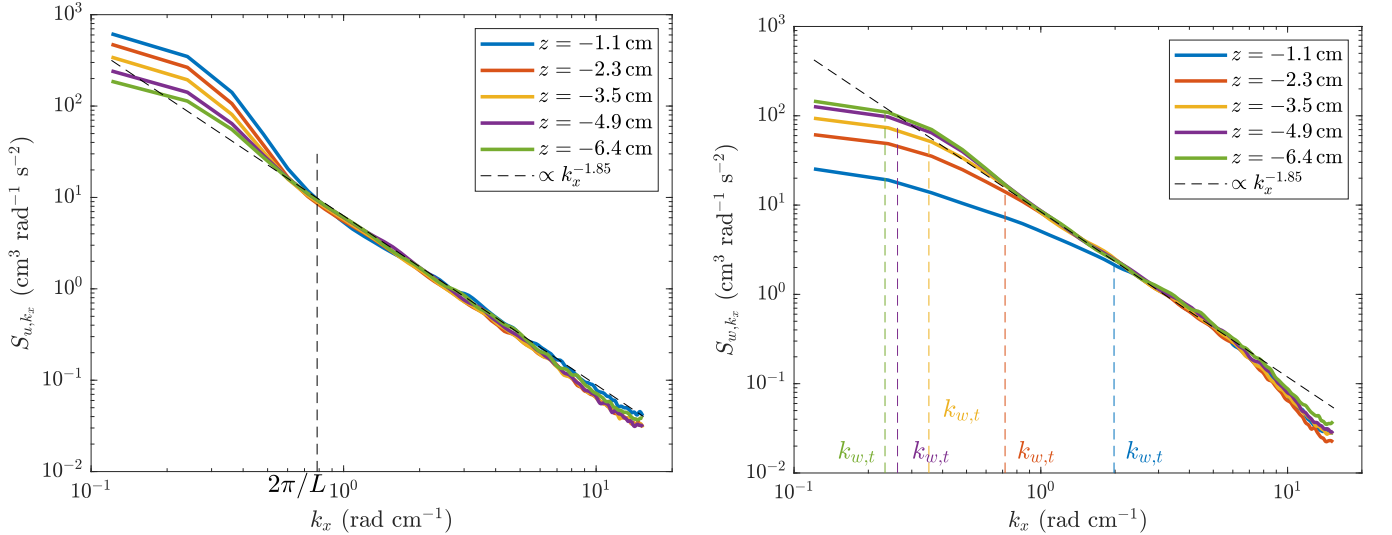


FIG. 13. (a) Longitudinal and (b) transverse spatial power spectra of horizontal and vertical turbulent velocity fluctuations  $S_{u,k_x}$  and  $S_{w,k_x}$  along  $x$  as functions of horizontal wavenumber  $k_x$  averaged over time for multiple depths and for  $y = 0$ . Dashed lines represent the same power law in  $k_x^{-1.85}$  and the same prefactor as in Fig. 9. Parameters of Experiment A.

the flow anisotropy also constitutes a surprising observation, which has been pointed out recently by Flores et al. [22]. Suppression at low wavenumbers or frequencies of the vertical velocity spectrum and extension of the power law spectrum for the horizontal component above the isotropic range have been reported only by few experimental studies with oscillating grids [8, 33], random actuated jets [9] or field measurements at a river surface [31].

Moreover, it should be noted that in our experiment, due to the finite size of our setup, the large-scale part of the horizontal spatial spectrum is affected by the significant horizontal inhomogeneity observed for horizontal velocity near the free surface in particular on the edges as illustrated in Fig. 3 (b). This induces an artificially enhanced longitudinal spectrum at large scales.



### C. Comparison of the experimental spectra with existing models

We discuss now the behavior of spatial and temporal spectra in the vicinity of the free surface with two approaches available in the literature. On one hand, the rapid distortion theory (RDT) proposes a partial explanation of these observations. It states that for eddies larger than the depth  $|z|$ , vertical velocity fluctuations are converted into horizontal ones [28], and the transverse spectral energy density for vertical velocity decreases while the longitudinal one for horizontal velocity increases. Accordingly, this theory predicts that both horizontal and vertical spatial spectra  $S_{u,k_x}$  and  $S_{w,k_x}$  remain unchanged near the free surface for small scales, i.e., for  $k_x \gtrsim 1/|z|$  [28, 66]. The same  $-5/3$  power law is then expected at these scales, a consequence of the structure of the turbulence in the isotropic and homogeneous region far from the surface. For larger scale ( $k_x \lesssim 1/|z|$ ), the amplitude of the longitudinal spectrum of horizontal velocities  $S_{u,k_x}$  is enhanced while  $S_{w,k_x}$  is strongly reduced. The latter reaches a plateau value evolving in  $z^{-5/3}$  for  $k_x \ll 1/L$  whereas the plateau value of the former stays the same.

On the other hand, Flores et al. [22] propose an alternative explanation by analogy with the stratified turbulence. Close to the free surface, vertical motions are inhibited whereas horizontal motions are strongly sheared. By dimensional analysis, the spectrum for the horizontal velocity reads  $S_{u,k_x} \sim C_h \epsilon^{2/3} k_x^{-5/3}$ , with  $\epsilon$  the local dissipation rate and  $C_h$  a constant prefactor which can differ from  $C'_\parallel$ . This spectrum is interpreted for stratified turbulence as a forward cascade transferring energy to small scale through nonlinear fluctuations of stratification and not between three-dimensional velocities eddies [74]. This situation differs from the two-dimensional turbulence, where the inverse cascade displays also a power law velocity spectrum in  $k_x^{-5/3}$  but corresponding to an upscale transfer of energy. Notice that contrary to the RDT where the inertial range near the free surface is linked to the one observed in the homogeneous region, the analogy with stratified turbulence makes this  $-5/3$  power law near the free surface specific to this layer and independent from the turbulent flow below. At the vicinity of the free surface, the cascade is controlled by the local dissipation rate which is enhanced by the strong vertical shearing of horizontal velocities. Direct numerical simulations of decaying turbulence near a stress-free surface of Flores et al. [22] may support this stratified-turbulence analogy, by computing the energy transfers through the scales. They also observe for wavenumbers smaller than the inverse of the fluid depth, a loss of isotropy, with a nearly constant spectrum of horizontal velocity  $S_{u,k_x}$ , whereas the vertical one  $S_{w,k_x}$  is strongly reduced. However, in their simulations, the stratified-like turbulence behavior occurs relatively close to the stress-free surface, i.e.,  $|z| < 0.1L$  when the vertical velocity becomes negligible, a region that is not studied in the present paper.

In our experimental measurements where the turbulence is continuously forced, we admittedly observe a clear enhancement of the amplitude of the longitudinal spectrum of horizontal velocity  $S_{u,k_x}$  at the vicinity of the free surface below a transition wavenumber  $k_{u,t} \approx 2\pi/L$  while the spectrum remains unchanged above  $k_{u,t}$  [see Fig. 13 (a)]. However, these observations for the horizontal longitudinal spectrum do not match the predictions of the RDT and of the analogy with the stratified turbulence. According to the RDT, the transition wavenumber  $k_{u,t}$  should be in  $1/|z|$ , whereas it remains nearly constant in our experiments. The region  $k_x \ll 1/L$  in which the RDT predicts an unchanged plateau is not spatially resolved in our experiments. But the enhancement of  $S_{u,k_x}$  we observe in the intermediate region ( $k_x \lesssim 1/|z|$ ) is expected according to the RDT but less markedly. Indeed, spectral power density is not supposed to be over  $S_{u,k_x}(k_x = 0, z = -\infty) = 2\sigma_u^2 L/\pi = 360 \text{ cm}^3 \text{ rad}^{-1} \text{ s}^{-2}$  for experiment A [28, 66], but we see in Fig. 13 (a) that  $S_{u,k_x}$  reaches values larger than  $600 \text{ cm}^3 \text{ rad}^{-1} \text{ s}^{-2}$  close to the free surface. These two disagreements between our experiments and the RDT may be explained by the lack of homogeneity of  $u$  close to the free surface [visible in Fig. 2 (a)], affecting the power spectrum at large scale.

Regarding the analogy with the stratified turbulence, the dissipation rate measured in the bulk should not apply to the cascade close to the free surface, because this analogy supposes that the local dissipation rate is reinforced by the strong vertical shearing of horizontal velocity [22]. But, as previously noted and illustrated in Figs. 13 (a) and 14, the spatial spectrum  $S_{u,k_x}$  and the time spectrum  $S_{u,\omega}$  of the horizontal velocity follow well the power laws established in homogeneous region using the same dissipation rate and the same prefactors as in the bulk. The same observation is reported in the simulations of Flores et al. [22].

Regarding the vertical velocity spectrum, our observations are in better agreement with the prediction of the RDT. Indeed, the transition wavenumber follows  $k_{w,t} \sim 1/|z|$  [see Fig. 12 (b)], above which the spectrum remains unchanged and below which the amplitude of the spectrum decreases. This agreement, contrasting with the behavior observed for horizontal velocity, may be due to the fact that the horizontal inhomogeneity is not observed for the vertical velocity [see Fig. 3 (b)]. We also note that the analogy with the stratified turbulence neglects the vertical velocity close to the free surface and does not provide any prediction for vertical velocity spectra.

To end this section, we emphasize that these two theoretical approaches addressing the turbulence close to a free surface cannot be applied directly to our experiments and also to the other measurements reported in the literature, because some of the hypotheses are not fully met. The RDT describes the evolution of an inviscid potential flow associated with decaying turbulence and treats only the geometrical effect of the free surface. The stratified-like

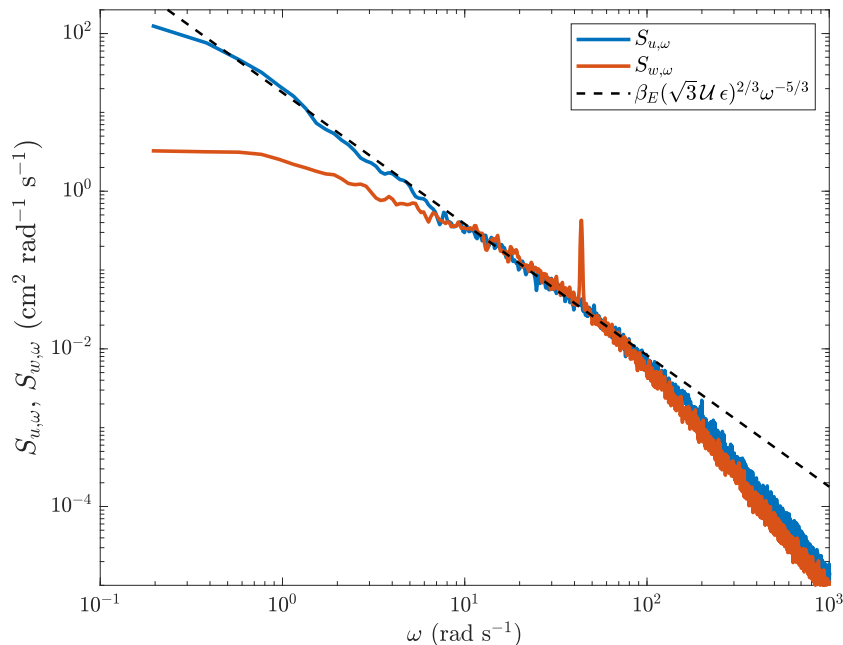


FIG. 14. Horizontal and vertical velocity temporal power spectra  $S_{u,\omega}$  and  $S_{w,\omega}$  as functions of the frequency  $\omega$  for  $x = 0$ ,  $y = -7$  cm and depths  $z = -1.0$  cm and  $z = -1.3$  cm, for horizontal and vertical velocities  $u$  and  $w$  respectively. Dashed line represents the same theoretical law predicted by Tennekes [58] choosing the same value  $\beta_E = 0.7$  as in Fig. 10. Duration: 1200 s.  $Q_j = 0.25$  L s $^{-1}$ .

turbulence region, where the vertical energy transfers become inhibited, seems limited to a very thin region ( $z < 0.1 L$ ), which is not resolved experimentally, although the spectra are already affected by the free surface. Moreover, the finite size of the experimental setups induces heterogeneity of the horizontal flows close to the free surface. In the absence of more appropriate models in the literature, we use the RDT and the analogy with the stratified turbulence for qualitative insights only.

#### D. Integral length scales near the free surface

We now study experimentally the behavior of integral length scales when approaching the free surface. The typical size of turbulent eddies is measured by computing, as the function of the vertical coordinate  $z$ , the longitudinal integral length  $L_{uu}$  for the horizontal velocity and the transverse one  $L_{ww}$  for the vertical velocity using the PIV measurements and the same methods as in Sect. III. We use normalized autocorrelation functions  $\rho_{uu}$  and  $\rho_{ww}$  as functions of longitudinal increment  $r_x$  and of depth  $z$  as defined in Sect. III A and Eq. (1). This study is qualitative only so we use the same curve fitting as in Sect. III A even though we are not in a homogeneous and isotropic region anymore. We show also that the use of an exponential fit for  $L_{uu}$  gives indeed similar results.

Figure 15 (a) displays  $\rho_{uu}$  and  $\rho_{ww}$  for  $z = -1.26$  cm which is the smallest depth for which full width is illuminated. For  $\rho_{ww}$ , even at large scales, we observe a significant correlation of about 0.1 of unknown physical origin. This may be due to the fact that  $w$  have low values near the free surface [see Fig. 11 (a)] thus artifacts or low-amplitude phenomena (e.g., setup mechanical oscillations, large scale currents) are more likely to be visible. As shown in Fig. 15 (b), this behavior disappears for  $z < -2$  cm, and curve fitting is then quite satisfying. Using these fitting curves, we compute  $L_{uu}$  and  $L_{ww}$  from  $\rho_{uu}$  and  $\rho_{ww}$  for various depths, which are displayed in Fig. 16.  $L_{uu}$  is also computed using a purely exponential fit of  $\rho_{uu}$  (crosses), showing the same qualitative behavior. We observe that  $L_{uu}$  increases near the free surface which is in strong disagreement with the decrease predicted by the RDT, where  $L_{uu}$  is predicted to slightly diminish to reach  $L_{uu}(z = 0) = 2/3 \tilde{L}_{uu}$  (due to the relation  $L_{uu} = \tilde{L}_{uu} \tilde{\sigma}_u^2 / \sigma_u^2$ ) [28, 66]. As for power-spectrum disagreement, this may be explained by the finite-size effects leading to horizontal inhomogeneity of  $u$  close to the free surface.

Besides,  $L_{ww}$  decreases experimentally when approaching the free surface. It is well predicted theoretically but with a lower rate than the predicted scaling  $L_{ww} \approx 1.96 |z|$  [66], which is unsurprising as this prediction is valid for  $z/L \ll 1$  only. We notice that when moving away from the turbulence-producing area,  $L_{uu}$  also increases in the

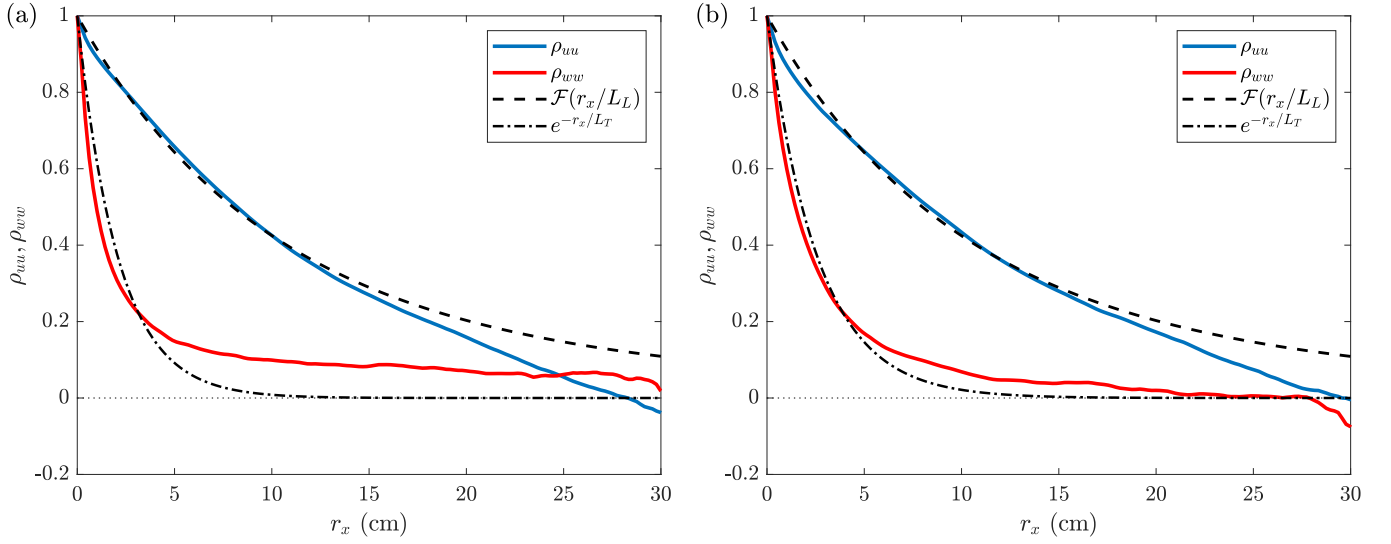


FIG. 15. Autocorrelation functions  $\rho_{uu}$  and  $\rho_{ww}$  (blue and red solid lines, respectively) of horizontal and vertical velocities  $u$  and  $w$  along  $x$  as functions of spatial increment  $r_x$ , like in Fig. 6 (a) but for two depths close to the free surface (a)  $z = -1.26$  cm and (b)  $z = -2.08$  cm. Curve fitting is also displayed with black dashed line representing  $\rho_{uu}$  from Eq. (3) and black dash-dotted line being an exponential fit of  $\rho_{ww}$ . Parameters of Experiment A;  $y = 0$ .

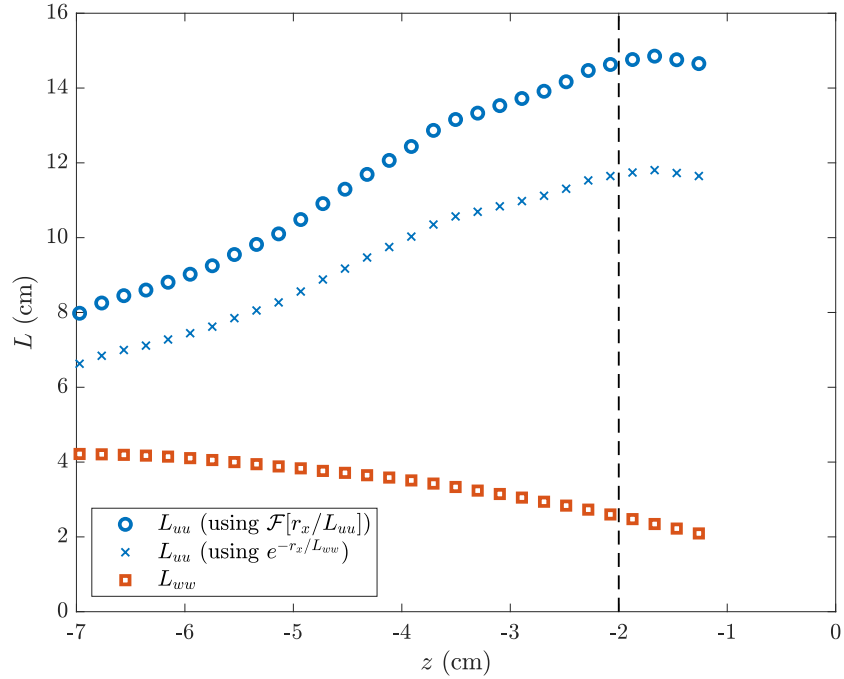


FIG. 16. Longitudinal ( $L_{uu}$ , circles) and transversal ( $L_{ww}$ , squares) integral length scales of horizontal and vertical velocities respectively as a function of depth  $z$ . Longitudinal integral length scale computed from exponential fit of  $\rho_{uu}$  is also plotted (crosses) for comparison. Parameters of Experiment A.

homogeneous and isotropic region ( $z < -6$  cm). This observation was also reported in grid-stirred experiments [33]. Further experimental, numerical, and theoretical studies are thus requested to understand the behavior of the local integral scale for turbulent flows in the vicinity of a free surface.

## V. CONCLUSION AND PERSPECTIVES

An original experimental device has been realized to generate and study turbulent water flows in the presence of a free surface in contact with the atmosphere, an omnipresent situation in nature. We propose an evolution of the random actuated jet array (RASJA) device, which is now commonly used to produce homogeneous and isotropic turbulence with a small mean flow. Here, instead of using an independent bilge pump for each jet, the jets are connected to a central powerful pump, whereas the jets can be independently turned on and off. At a given time 16 jets over 64 fire simultaneously with a typical opening time of 3 s and a random choice of the position and of the opening duration. Using this protocol in a glass tank of dimensions  $40 \times 40 \times 75$  cm and filled up to a water depth of 66 cm, we characterize the properties of the turbulent flow mainly using PIV measurements in a vertical plane below the free surface. For a fluid depth larger than the integral length and sufficiently far from the jets, i.e., in the range  $-9 < z < -6$  cm, we recover the properties of homogeneous and isotropic turbulence, whose intensity can be adjusted over one order of magnitude by changing the flow rate of the central pump. In this region, we report a good isotropy and horizontal homogeneity of the velocity fluctuations. Turbulent flows significantly stronger than in the other random actuated jet arrays are produced, as we reach at the maximum a turbulent Reynolds number  $Re_T = 8801$ , a Taylor Reynolds number  $Re_\lambda = 558$  and a dissipation rate  $\epsilon = 71 \text{ cm}^2 \text{ s}^{-3}$ . The turbulent fluctuations increase linearly with the flow rate per jet, vary between 1 and  $11 \text{ cm s}^{-1}$  and remain at least three times larger than the local values of the mean flow. Moreover, we observe that the integral length scale  $L$  (assimilated to the longitudinal one) is not significantly affected by the forcing amplitude and remains close to 8 cm, a length which seems imposed by the geometry of the jet array and of the water tank. Therefore, the turbulent intensity can be varied without changing too much the large-scale structure. Our experimental device thus proposes an efficient facility to study fundamental homogeneous isotropic turbulence without a large mean flow in the laboratory. Turbulent transport of particles or multiphase flows could also be investigated.

The modification of the properties of the turbulence by an air-water top-free surface constitutes the first application of our facility. Despite the ubiquity of this situation in nature, this problem has been investigated in few experiments, mainly to quantify the gas exchanges with the atmosphere. As stated by Variano and Cowen [45], the RASJA experiments, compared to grid stirred tanks [8, 33, 36, 37], generate a stronger level of turbulence, have a better reproducibility and are less subjected to large scale circulations due to the oscillation of the grids. They constitute the best method to investigate free-surface turbulence in the absence of a large mean flow. With our experimental setup, we observe the modification of the turbulent flow near the free surface on a depth of order the integral length, i.e., in the domain  $-6 < z < 0$  cm. The deformations of the free surface by the subsurface turbulence will be studied in dedicated forthcoming work and remain sufficiently small in first approximation (below 2 mm) to treat the free surface as a rigid flat wall. The turbulence becomes strongly anisotropic when approaching the free surface, with a decay of the vertical velocity fluctuations and an enhancement of horizontal ones. The application of the rapid distortion theory (RDT) for shear-free turbulence near a wall initially proposed by Hunt and Graham [28, 66] and improved by Magnaudet and Calmet [19, 30] describes satisfyingly the experimental profile of the vertical velocity fluctuations using the turbulent parameters measured in the homogeneous isotropic region. We also report a predicted increase of the horizontal velocity fluctuations but reaching a maximum located about 1 cm below the free surface, not predicted theoretically. The horizontal velocity increase is also larger than the one predicted by the RDT. This observation, also reported in some previous numerical simulations [26], does not have to date a satisfying theoretical explanation. In our case, this may be explained by finite size effects, observed near the free surface and leading to a concentration of horizontal velocity fluctuations in the horizontal center of the tank.

The modification of velocity power spectra  $S_{u,k_x}$  and  $S_{w,k_x}$  due to the free surface have also been investigated. At small scales, despite the anisotropy and the inhomogeneity of the flow, the velocity power spectra satisfyingly follow a power law in  $k^{-1.85}$  like for homogeneous and isotropic turbulence and with the same parameters, suggesting that the small turbulent eddies remain unaffected by the free surface. Consistently with the decay of vertical velocity fluctuations for increasing  $z$ , the vertical velocity power spectrum  $S_{w,k_x}$  displays also a smaller value at large scales, in agreement with the predictions of the RDT. The transition between large-scale and small-scale behaviors occurs for a transition wavenumber  $k_{w,t} \sim 1/|z|$  which is also predicted. In contrast, the horizontal velocity power spectrum  $S_{u,k_x}$  is amplified at large scales, i.e.,  $k_x \lesssim 2\pi/L$ . The RDT predicts this increase but with a lesser amplitude and the predicted transition between large scale and small scale behaviors is predicted to occur at a wavenumber  $k_{u,t} \sim 1/|z|$ . The temporal spectrum  $S_{u,\omega}$  measured locally by LDV shows that the turbulent cascade in  $\omega^{-5/3}$  spreads at larger scales, as pointed out by Flores et al. [22].

Finally, we show experimentally a clear increase of the horizontal longitudinal integral scale when approaching the free surface, as well as a decrease of the vertical transverse integral scale. The former observation is in contradiction with the RDT which predicts a decrease of the horizontal longitudinal integral scale.

To conclude, when analyzing our results close to the free surface, we confirm predictions from the RDT regarding vertical velocity fluctuations when approaching the free surface: the quantitative evolution of  $\sigma_w$ , the decrease of

the power spectrum  $S_{w,k_x}$  at large scales and its constancy at small scales, as well as the transition wavenumber  $k_{w,t} \sim 1/|z|$  between these two parts, and the qualitative decrease of the transverse vertical integral scale. Regarding horizontal velocity fluctuations, we have discrepancies between our experimental data and RDT, quantitatively for some aspects (evolution of  $\sigma_u$  and of large scale spatial power spectrum), but even qualitatively (evolution of transition wavenumber  $k_{u,t}$  and of longitudinal horizontal integral scale). We explain these differences mainly by finite-size effects, the boundaries concentrating horizontal velocity energy in the center of the tank. Besides, the RDT assumes the linear deformation of a “frozen” potential flow due to geometrical obstacles and neglects any viscous effects, while the impingement of turbulent structures from below feeds continuously the surface turbulence and we may expect nonlinearities. Indeed, the emergence of intense turbulence and of large-scale circulations appears as a consequence of the strong anisotropy leading to nearly two-dimensional flows. The free surface is also modeled as a stress-free interface but with no deformation. Therefore, unsurprisingly, this theory cannot accurately describe the turbulence close to a free surface, whereas this is the only theoretical work applicable to our measurements to our knowledge. Further experimental, numerical, and theoretical work would thus be helpful to understand the action of a free surface on hydrodynamics turbulence.

### ACKNOWLEDGMENTS

We gratefully thank Alexandre Lantheaume, Yann Le Goas, David Charalampous, Arnaud Grados, Alexandre Di Palma, Laurent Réa, Stefano Lun Kwong and Mathieu Receveur for technical assistance and help in the conception and building of the experimental device. We acknowledge the Sphynx group at CEA, France for lending a LDV apparatus for the first set of experiments. We are also indebted to Evan Variano (UC Berkeley) for advises and discussions about RASJA experiments. This work was funded by the French National Research Agency (ANR TURBULON project No. ANR-12-BS04-0005 and ANR DYSTURB project No. ANR-17-CE30-0004). T. Jamin was partially supported by the DGA (Direction Generale de l’Armement, France) and the CNRS.

- 
- [1] H. Tennekes and J. L. Lumley, *A First Course in Turbulence* (The MIT Press, 1972).
  - [2] U. Frisch, *Turbulence: The Legacy of A. N. Kolmogorov* (Cambridge University Press, 1995).
  - [3] S. B. Pope, *Turbulent Flows* (Cambridge University Press, USA, 4th edition, 2006).
  - [4] C. Bailly and G. Comte-Bellot, *Turbulence* (Springer, Switzerland, 2015).
  - [5] M. Brocchini and D. H. Peregrine, The dynamics of strong turbulence at free surfaces. Part 1. Description, *J. Fluid Mech.* **449**, 225 (2001).
  - [6] S. A. Thorpe, Dynamical processes of transfer at the sea surface, *Prog. Oceanogr.* **35**, 315 (1995).
  - [7] F. Veron, W. K. Melville, and L. Lenain, Measurements of ocean surface turbulence and wave-turbulence interactions, *J. Phys. Oceanogr.* **39**, 2323 (2009).
  - [8] H. Herlina and G. H. Jirka, Experiments on gas transfer at the air-water interface induced by oscillating grid turbulence, *J. Fluid Mech.* **594**, 183 (2008).
  - [9] E. A. Variano and E. A. Cowen, Turbulent transport of a high-Schmidt-number scalar near an air-water interface, *J. Fluid Mech.* **731** 259 (2013).
  - [10] H. Herlina and J. G. Wissink, Simulation of air-water interfacial mass transfer driven by high-intensity isotropic turbulence, *J. Fluid Mech.* **860**, 419 (2019).
  - [11] Y. Pan and S. Banerjee, A numerical study of free-surface turbulence in channel flow, *Phys. Fluids* **7**, 1649 (1995).
  - [12] L. Shen and D. K. P. Yue, Large-eddy simulation of free-surface turbulence, *J. Fluid Mech.* **440** 75 (2001).
  - [13] H. Yoshimura and I. Fujita, Investigation of free-surface dynamics in an open-channel flow, *J. Hydraul. Res.*, **58**, 231 (2019).
  - [14] S. Kumar, R. Gupta, and S. Banerjee, An experimental investigation of the characteristics of free-surface turbulence in channel flow, *Phys. Fluids* **10**, 437 (1998).
  - [15] R. Savelsberg and W. van de Water, Turbulence of a free surface, *Phys. Rev. Lett.* **100**, 034501 (2008).
  - [16] R. Savelsberg and W. van de Water, Experiments on free-surface turbulence, *J. Fluid Mech.* **619**, 95 (2009).
  - [17] G. Dolcetti, K. V. Horoshenkov, A. Krynkina, and S. J. Tait, Frequency-wavenumber spectrum of the free surface of shallow turbulent flows over a rough boundary, *Phys. Fluids* **28**, 105105 (2016).
  - [18] B. Perot and P. Moin, Shear-free turbulent boundary layers. Part 1. Physical insights into near-wall turbulence, *J. Fluid Mech.* **295**, 199 (1995).
  - [19] I. Calmet and J. Magnaudet, Statistical structure of high-Reynolds-number turbulence close to the free surface of an open-channel flow, *J. Fluid Mech.* **474**, 355 (2003).
  - [20] G. Campagne, J.-B. Cazalbou, L. Joly, and P. Chassaing, The structure of a statistically steady turbulent boundary layer near a free-slip surface, *Phys. Fluids* **21**, 065111 (2009).

- [21] H. Herlina and J. G. Wissink, Direct numerical simulation of turbulent scalar transport across a flat surface, *J. Fluid Mech.* **744**, 217 (2014).
- [22] O. Flores, J. J. Riley, and A. Horner-Devine, On the dynamics of turbulence near a free surface, *J. Fluid Mech.* **821**, 248 (2017).
- [23] L. Shen, D. K. P. Yue, and G. S. Triantafyllou, Effect of surfactants on free-surface turbulent flows, *J. Fluid Mech.* **506**, 79 (2004).
- [24] J. Bodart, J.-B. Cazalbou, and L. Joly, Direct numerical simulation of unshered turbulence diffusing towards a free-slip or no-slip surface, *J. Turbul.* **11**, 1 (2010).
- [25] J. G. Wissink, H. Herlina, Y. Akar, and M. Uhlmann, Effect of surface contamination on interfacial mass transfer rate, *J. Fluid Mech.* **830**, 5 (2017).
- [26] X. Guo and L. Shen, Interaction of a deformable free surface with statistically steady homogeneous turbulence, *J. Fluid Mech.* **658**, 33 (2010).
- [27] X. Yu, K. Hendrickson, B. K. Campbell, and D. K. P. Yue, Numerical investigation of shear-flow free-surface turbulence and air entrainment at large Froude and Weber numbers, *J. Fluid Mech.* **880**, 209 (2019).
- [28] J. C. R. Hunt and J. M. R. Graham, Free-stream turbulence near plane boundaries, *J. Fluid Mech.* **84**, 209 (1978).
- [29] M. A. C. Teixeira and S. E. Belcher, Dissipation of shear-free turbulence near boundaries, *J. Fluid Mech.* **422**, 167 (2000).
- [30] J. Magnaudet, High-Reynolds-number turbulence in a shear-free boundary layer: revisiting the Hunt-Graham theory, *J. Fluid Mech.* **484**, 167 (2003).
- [31] C. C. Chickadel, S. A. Talke, A. R. Horner-Devine, and A. T. Jessup, Infrared-based measurements of velocity, turbulent kinetic energy, and dissipation at the water surface in a tidal river, *IEEE Geosci. Remote S.* **8**, 849 (2011).
- [32] S. A. Talke, A. R. Horner-Devine, C. C. Chickadel, and A. T. Jessup, Turbulent kinetic energy and coherent structures in a tidal river, *J. Geophys. Res. Oceans* **118**, 6965 (2013).
- [33] B. H. Brumley and G. H. Jirka, Near-surface turbulence in a grid-stirred tank, *J. Fluid Mech.* **183**, 235 (1987).
- [34] S. M. Thompson and J. S. Turner, Mixing across an interface due to turbulence generated by an oscillating grid, *J. Fluid Mech.* **67**, 349 (1975).
- [35] S. I. Badulin, S. I. Voropayev, A. V. Kulikov, and A. D. Rozenberg, Effect of turbulence on low-amplitude regular gravity waves, *Oceanology* **28**, 429 (1988).
- [36] S. P. McKenna and W. R. McGillis, The role of free-surface turbulence and surfactants in air-water gas transfer, *Int. J. Heat Mass Transfer* **47**, 539 (2004).
- [37] L. Chiapponi, S. Longo, and M. Tonelli, Experimental study on oscillating grid turbulence and free surface fluctuation, *Exp. Fluids* **53**, 1515 (2012).
- [38] S. P. McKenna, Free-surface turbulence and air-water gas exchange, PhD thesis, Massachusetts Institute of Technology, USA, (2000).
- [39] S. Douady, Y. Couder, and M. E. Brachet, Direct observation of the intermittency of intense vorticity filaments in turbulence, *Phys. Rev. Lett.* **67**, 983 (1991).
- [40] S. Fauve, C. Laroche, and B. Castaing, Pressure fluctuations in swirling turbulent flows, *J. Phys. II France* **3**, 271 (1993).
- [41] F. Ravelet, A. Chiffaudel, and F. Daviaud, Supercritical transition to turbulence in an inertially driven von Kármán closed flow, *J. Fluid Mech.* **601**, 339 (2008).
- [42] A. Cazaubiel, J.-B. Gorce, J.-C. Bacri, M. Berhanu, C. Laroche, and E. Falcon, Three-dimensional turbulence generated homogeneously by magnetic particles, *Phys. Rev. Fluids* **6**, L112601 (2021); J.-B. Gorce and E. Falcon, Statistical Equilibrium of Large Scales in Three-Dimensional Hydrodynamic Turbulence, *Phys. Rev. Lett.* **129**, 054501 (2022).
- [43] P. Gutiérrez and S. Aumaître, Surface waves propagating on a turbulent flow, *Phys. Fluids* **28**, 025107 (2016).
- [44] E. A. Variano, E. Bodenschatz, and E. A. Cowen, A random synthetic jet array driven turbulence tank, *Exp. Fluids* **37**, 613 (2004).
- [45] E. A. Variano and E. A. Cowen, A random-jet-stirred turbulence tank, *J. Fluid Mech.* **604**, 1 (2008).
- [46] W. Hwang and J. K. Eaton, Creating homogeneous and isotropic turbulence without a mean flow, *Exp. Fluids* **36**, 444 (2004).
- [47] G. Bellani and E. A. Variano, Homogeneity and isotropy in a laboratory turbulent flow, *Exp. Fluids* **55**, 1646 (2014).
- [48] D. Carter, A. Petersen, O. Amili, and F. Coletti, Generating and controlling homogeneous air turbulence using random jet arrays, *Exp. Fluids* **57**, 189 (2016).
- [49] B. A. Johnson and E. A. Cowen, Turbulent boundary layers absent mean shear, *J. Fluid Mech.* **835**, 217 (2018).
- [50] L. Blay Esteban, J. S. Shrimpton, and B. Ganapathisubramani, Laboratory experiments on the temporal decay of homogeneous anisotropic turbulence, *J. Fluid Mech.* **862**, 99 (2019).
- [51] A. Pérez-Alvarado, L. Mydlarski, and S. Gaskin, Effect of the driving algorithm on the turbulence generated by a random jet array, *Exp. Fluids* **57**, 20 (2016).
- [52] J. George, F. Minel, and M. Grisenti, Physical and hydrodynamical parameters controlling gas-liquid mass transfer, *Int. J. Heat Mass Transfer* **37**, 1569 (1994).
- [53] F. Minel and J. George, Hydrodynamics in a jet-agitated vessel close to the gas-liquid surface, In B. Jähne and E. C. Monahan, editors, *Air-Water Gas Transfer*, pages 665-673. AEON Verlag and Studio, 63454 Hanau, (1995).
- [54] Private communication with Evan A. Variano.
- [55] S. Delbos, V. Weitbrecht, T. Bleninger, P. P. Grand, E. Chassaing, D. Lincot, O. Kerrec, and G. H. Jirka, Homogeneous turbulence at an electrodeposition surface induced by randomly firing jet arrays, *Exp. Fluids* **46**, 1105 (2009).
- [56] T. Jamin, Interactions between free-surface waves and hydrodynamic flows, PhD thesis, Université Paris Diderot, (2016).
- [57] W. Thielicke and E.J. Stamhuis, PIVlab - Towards user-friendly, affordable and accurate digital particle image velocimetry

in Matlab, *J. Open Res. Softw.* **2**, e30 (2014).

- [58] H. Tennekes, Eulerian and Lagrangian time microscales in isotropic turbulence, *J. Fluid Mech.* **67**, 561 (1975).
- [59] K. R. Sreenivasan, On the universality of the Kolmogorov constant, *Phys. Fluids* **7**, 2778 (1995).
- [60] D. W. Carter and F. Coletti, Scale-to-scale anisotropy in homogeneous turbulence, *J. Fluid Mech.* **827**, 250 (2017).
- [61] The turbulent Reynolds numbers reported for grid-stirred tanks are divided by two according to the definition of the turbulent Reynolds number in this article.
- [62] R. Zimmermann, H. Xu, Y. Gasteuil, M. Bourgoin, R. Volk, J.-F. Pinton, and E. Bodenschatz, The Lagrangian exploration module: An apparatus for the study of statistically homogeneous and isotropic turbulence, *Rev. Sci. Instrum.* **81**, 055112 (2010).
- [63] M. López-Caballero and J. Burguete, Inverse cascades sustained by the transfer rate of angular momentum in a 3D turbulent flow, *Phys. Rev. Lett.* **110**, 124501 (2013).
- [64] A. Sanchis and A. Jensen, Dynamic masking of PIV images using the radon transform in free surface flows, *Exp. Fluids* **51**, 871 (2011).
- [65] T. Jamin, L. Gordillo, G. Ruiz-Chavarría, M. Berhanu, and E. Falcon, Experiments on generation of surface waves by an underwater moving bottom, *Proc. R. Soc. A* **471**, 20150069 (2015).
- [66] J. C. R. Hunt, Turbulence structure in thermal convection and shear-free boundary layers, *J. Fluid Mech.* **138**, 161 (1984).
- [67] J. Lucassen, Longitudinal capillary waves. Part 1. Theory, *Trans. Faraday Soc.* **64**, 2221 (1968).
- [68] W. G. Van Dorn, Boundary dissipation of oscillatory waves, *J. Fluid Mech.* **24**, 769 (1966).
- [69] J. W. Miles, Surface-wave damping in closed basins, *Proc. R. Soc. A* **297**, 459 (1967).
- [70] D. M. Henderson and J. W. Miles, Single-mode Faraday waves in small cylinders, *J. Fluid Mech.* **213**, 95 (1990).
- [71] J. L. Hammack and D. M. Henderson, Resonant interactions among surface water waves, *Annu. Rev. Fluid Mech.* **25**, 55 (1993).
- [72] N. M. Frew, E. J. Bock, U. Schimpf, T. Hara, H. Haußecker, J. B. Edson, W. R. McGillis, R. K. Nelson, S. P. McKenna, B. M. Uz, and B. Jähne, Air-sea gas transfer: Its dependence on wind stress, small-scale roughness, and surface films, *J. Geophys. Res.* **109**, C08S17 (2004).
- [73] E. L. G. Kit, E. J. Strang, and H. J. S. Fernando, Measurement of turbulence near shear-free density interfaces, *J. Fluid Mech.* **334**, 293 (1997).
- [74] E. Lindborg, The energy cascade in a strongly stratified fluid, *J. Fluid Mech.* **550**, 207 (2006).